

Effect of corner radius on flow topology and heat transfer from free oscillating tandem cylinders at low Reynolds number

Cite as: Phys. Fluids **35**, 013607 (2023); <https://doi.org/10.1063/5.0132185>

Submitted: 27 October 2022 • Accepted: 28 December 2022 • Accepted Manuscript Online: 28 December 2022 • Published Online: 19 January 2023

 Yuvraj Sarout,  Md Islam,  Yap Yit Fatt, et al.



View Online



Export Citation



CrossMark

ARTICLES YOU MAY BE INTERESTED IN

[External force attached binding focus of particles and its application](#)

Physics of Fluids **35**, 012016 (2023); <https://doi.org/10.1063/5.0131077>

[Heat transfer and wake-induced vibrations of heated tandem cylinders with two degrees of freedom: Effect of spacing ratio](#)

Physics of Fluids **34**, 113612 (2022); <https://doi.org/10.1063/5.0124772>

[Flow-mediated interaction between a forced-oscillating cylinder and an elastically mounted cylinder in less regular regimes](#)

Physics of Fluids **35**, 013608 (2023); <https://doi.org/10.1063/5.0132212>



Physics of Fluids

Special Topic: Paint and Coating Physics

Submit Today!

Effect of corner radius on flow topology and heat transfer from free oscillating tandem cylinders at low Reynolds number

Cite as: Phys. Fluids **35**, 013607 (2023); doi: 10.1063/5.0132185

Submitted: 27 October 2022 · Accepted: 28 December 2022 ·

Published Online: 19 January 2023



View Online



Export Citation



CrossMark

Yuvraj Sarout, Md Islam, ^{a)} Yap Yit Fatt, and Isam Janajreh

AFFILIATIONS

Khalifa University of Science and Technology, Abu Dhabi, United Arab Emirates

^{a)} Author to whom correspondence should be addressed: didarul.islam@ku.ac.ae and mdislam02@yahoo.com

ABSTRACT

Flow-induced vibration (FIV) on two tandem cylinders with forced convection is numerically investigated at a constant $Re = 150$. Elastically mounted cylinder with four different values of corner radii ($r^* = r/R$; r = radius of fillet; R = radius of circle) = 0 (square cylinder), 0.25, 0.75, and 1 (circular cylinder) with two spacing ratio (L/D) = 4 and 2 is studied. Transverse oscillations are generated from the cylinder having non-dimensional mass (m^*) = 10. The structural damping coefficient is assigned a zero value with varying reduced velocity $Ur = 2 - 10$. The two-dimensional incompressible Navier–Stokes and energy equations are solved together with Newton’s second law governing the motion of the cylinders. Both cylinders’ surfaces are maintained at a higher constant temperature of $T^* = 1$, and incoming flow is set to be at $T^* = 0$ with Prandtl number (Pr) = 0.7. The effect of r^* and L/D is observed on the flow structure and FIV parameters. Flow characteristics at $L/D = 4$ such as steady flow, reattachment, and unsteady flow are examined. A “shift” in vibrational amplitude is noted from $r^* = 1$ and 0.75 to $r^* = 0$ and 0.5, respectively. The downstream cylinder (D_C) experiences a hike in vibration amplitude due to the impingement of vortex shedding from the upstream cylinder (U_C). $r^* = 1$ has 18.1% higher vibrational amplitude than $r^* = 0$ at their respective lock-in regimes for D_C . For $L/D = 2$, vortices from upstream and downstream cylinders interact to form C(2S) and 2S types of vortex shedding. Different regimes, such as single body, reattachment, and co-shedding, have been observed while changing L/D . $r^* = 0.75$ results in 13.3% higher oscillation amplitude as compared to $r^* = 0.5$ for D_C . The average Nusselt number (Nu_{avg}) strongly depends on flow topology, corner radius, and vibrational amplitude A/D . At low L/D , heat transfer from the downstream cylinder is plummeted due to rolling of shear layers over the cylinder. There is a significant change in Nu_{avg} due to higher vibration; for example, increase in 10.71% change is observed from $Ur = 2$ to $Ur = 6$ for $r^* = 1$ and $L/D = 4$. Corner radii also alter the Nu_{avg} as a decrease in 27.39% from $r^* = 1$ to $r^* = 0$ at $Ur = 10$ and $L/D = 4$ (U_C).

Published under an exclusive license by AIP Publishing. <https://doi.org/10.1063/5.0132185>

NOMENCLATURE

A	Maximum amplitude (m)
c	Damping coefficient (N s/m)
c_p	Specific heat capacity (J/kg K)
C_L	Coefficient of lift
C_D	Average coefficient of drag
C_D^{\max}	Maximum coefficient of drag
D	Diameter of cylinder (m)
D_C	Downstream cylinder (m)
f_{mod}	Modulation frequency (s^{-1})
f_n	Natural frequency (s^{-1})
f_s, f^*	Frequency of oscillation (s^{-1})

F_n	Normalized natural frequency
k	Spring constant (N/m)
m	Mass (kg)
m^*	Mass ratio
NHc	Non-heated cylinder
Nu	Nusselt number
Nu_{avg}	Average Nusselt number
p	Pressure (Pa)
Pr	Prandtl number
$r^* = \frac{r}{R}$	Corner radii (r is the radius of the corner, R is the radius of the Cylinder)
Re	Reynolds number
Ri	Richardson number

T_s	Surface temperature (K)
T_∞	Flow temperature (K)
St	Strouhal number
u	x -velocity
U_C	Upstream cylinder
U_∞	Free stream velocity (m/s)
Ur	Reduced velocity
v	y -velocity
Y^*	Y -direction amplitude
λ	Thermal conductivity (W/m K)
μ	Viscosity (Pa s)
ξ	Damping ratio
ρ	Density (kg/m ³)

I. INTRODUCTION

Flow-induced vibration (FIV) is found to affect the structural integrity of marine structures (Xu *et al.*, 2022), heat exchangers (Cheng *et al.*, 2009; Ji *et al.*, 2022; and Qiu *et al.*, 2021), ocean pipelines (Ali *et al.*, 2022b; Gray *et al.*, 2015; and Rao *et al.*, 2017), and transmission lines (Gao *et al.*, 2021; Zhu *et al.*, 2019). FIV on an isolated bluff body, for example, single cylinder, has been investigated in existing kinds of literature (Williamson and Govardhan, 2004; Jauvtis and Williamson, 2003). For a single elastically mounted cylinder, its motion under a cross-flow configuration is governed by various factors including spring constant (k), damping constant (c), and natural frequency (f_n) (Chaplin *et al.*, 2005; Liu *et al.*, 2020). For a cylinder in cross-flow configuration, vortex shedding can generate vibrations if Re is not very low (Wang *et al.*, 2017; Xiao *et al.*, 2011). Williamson and Roshko (1988) divided vortex shedding type on the basis of amplitude-phase graph. High-amplitude vibration occurs when vortex shedding frequency (f_s) approaches f_n . This phenomenon is known as “lock-in synchronization” or “frequency synchronization” (Nepali *et al.*, 2020; Sarpkaya, 2004). Khalak and Williamson (1997) studied the effect of combined mass-damping ($m^*\xi$) on vortex shedding and amplitude modes. In the amplitude-phase graph, higher mass ratio is associated with the “initial” (2S vortex shedding mode, two singlets in a single period) and “lower” (2P vortex shedding mode, two pairs in single period) branches. However, in low mass ratio, lock-in region increases, and an “upper” branch appears. Low mass ratio leads to a broader lock-in region with only one “upper branch” of 2P vortex shedding mode.

FIV on two bluff bodies, for example, tandem cylinders, is a complex phenomenon. It is of course physically more interesting than FIV on a single cylinder. For tandem cylinders, the motions of both cylinders are intimately coupled through the hydrodynamic forces (Borazjani and Sotiropoulos, 2009; Mussa *et al.*, 2009). FIV on two tandem cylinders can be classified into different regimes based on the vibration amplitude and flow pattern observed. Systematic study of flow around tandem cylinders gives deep insight into flow structure. Different in spacing ratio L/D (L : center to center distance; D : diameter) results in different vibration regimes: single-body regime, reattachment regime, and co-shedding regime (Zdravkovich, 1996; 1987; Zhou and Mahbub Alam, 2016). For $L/D < 2.5$, single-body regime exists when both cylinders act as if they are an isolated bluff body in flow. For $2.5 < L/D < 5$, flow separation occurring from upstream cylinder (U_C) reattaches on the downstream cylinder (D_C), referred to as reattachment regime. For large spacing $L/D > 5$, vortices are shed

independently from each cylinder and are referred to as the co-shedding regime (Khan *et al.*, 2022; Sumner, 2010). For large spacing ratio, wake galloping and hitting of vortices generated from the U_C on the D_C are observed (Griffith *et al.*, 2017; Prasanth and Mittal, 2009). Lin *et al.* (2014) numerically investigated the effect of varying $m^* = 0.5 - 4$ and $Re = 5 - 100$ on isolated and tandem cylinders. In addition, the symmetrical vibration regime, an exceptional regime, is observed for tandem cylinders. Asymmetrical regime has been discovered even at low $Re = 10$ and $Ur > 7$. In the asymmetrical regime, the oscillation axes shift from the initial position and a “shift” occurs.

The above-cited studies were performed on circular cylinders, which is a special case of square cylinder with filleted corner radius exactly equal to half of its side length. More generally, for square cylinders, the sharp corners can be filleted to a specific corner radius to control flow separation location with the aim to alter the hydrodynamic forces and therefore mitigate FIV. For a square cylinder, flow separation generally occurs at the leading and trailing edges (Hu *et al.*, 2006; Kumar and Sen, 2021; and Sarout *et al.*, 2022b). As the sharp corners are rounded off, flow separation location changes due to the Coanda effect. For flow around a single square cylinder, Ajith Kumar *et al.* (2009) conducted a study on the influence of corner radius experimentally. The experiment was performed on six different $r^* = 0.0 - 0.5$ (where $r^* = r/R$ with corner radius r and half side length of a square cylinder R) in a water channel at $Re = 5200$. Sarout *et al.* (2022a) numerically investigated the effect of $r^* = 0 - 1$ and $Re = 100, 150$, and 200 on flow characteristics. Four different modes were observed; low-amplitude mode, beating mode, lock-in mode, and monotonic oscillation mode. The effect of r^* manifested clearly in the shedding regime and shedding cycle timing. Zhao and Zhao (2019) numerically examined the effect of r^* within the range of 0 to 0.5 on vibration modes at a constant $Re = 200$ where galloping and lock-in were observed. Galloping was completely suppressed for $r^* = 0.1$. Amplitude for lock-in increased due to a change in r^* from 0 and 0.5. In further analysis, beating was divided into two parts: type A and type B. In another study, Miran and Sohn (2015) numerically investigated the effect of corner radius of a square cylinder at $Re = 500$ for transient two-dimensional (2D) laminar with turbulence treated via large-eddy simulations. Six different $r^* = 0.0 - 0.5$ were examined for its effect on St . For r^* within the range of 0 to 0.2, a huge leap in St is registered and then gradually rose for the range of $0.2 < r^* < 0.5$. Sen and Mittal (2011) numerically investigated flow around a square cylinder with for Re in the range of $60 < Re < 250$. Three main regimes were observed with increase in Re : primary lock-in, desynchronization, and secondary lock-in. 2S type of vortex shedding was observed in initial branch. In lower branch, both 2S and C(2S) are detected. Vortex shedding in secondary lower branch was through 2S and 2P modes. Zhao *et al.* (2014) experimentally studied the effect of square cylinder angle of attack $\alpha = 0^\circ, 20^\circ$, and 45° with varying U_∞ . During the study, the effect of α and Ur on different five regimes was observed. For flow around filleted tandem cylinders, Adebbe *et al.* (2018) employed immersed-boundary lattice Boltzmann method to address the effect of r^* in the range of 0.1–0.5 and $L/D = 1.5 - 10$ at $Re = 100$. L/D and r^* affected both the separation and reattachment points with changes in flow regimes.

The interaction of flow with other factors such as heat transfer and structural elasticity might be crucial in understanding the FIV mechanism and mitigating the damage it causes. The most prevalent natural phenomena are heat transfer. A detailed review can be found

in Ali *et al.* (2021); Derakhshandeh and Alam (2019). Flow around heated cylinder with FIV demonstrates new findings, which govern the nature of temperature variation around the cylinder by Sun *et al.* (2021). Geometrical shape is a major factor in changing topology of flow around the cylinder and heat transfer phenomenon. Alam *et al.* (2021) numerically investigated the flow heat transfer over a fillet cylinder at $Re = 40\text{--}180$. For $r^* = 0.0\text{--}1.0$, flow topology, aerodynamics forces, and heat transfer were explored with four main flow patterns: steady trailing-edge separated flow, unsteady trailing-edge separated flow, unsteady separation-bubble flow, and unsteady leading-edge separated flow. Alam *et al.* (2021) reported the effect of corner radius and the angle of attack α on heat transfer at a constant $Re = 150$. For Corner radius in the range of $r^* = 0\text{--}1$, α is varied from 0° to 45° . With varying r^* and α , four flow patterns were explored: A, B, C, and D. Change in heat transfer due to mainly ascribed variations in the boundary layer, side-surface bubble, primary wake bubble, and secondary wake bubble. Mahir and Altaç (2008) numerically investigated the heat transfer in laminar unsteady flow around tandem cylinders at $Re = 100$ and 200 . For varying $L/D = 2\text{--}10$, Nu_{avg} was obtained for U_C and D_C . At higher spacing ratios $L/D > 4$, U_C acts as an isolated cylinder. Dwivedi and Dhiman (2019) numerically inspected heat transfer and flow interaction between tandem cylinders at $Re = 100$ and $Pr = 0.7$. Energy equation was solved for five different $L/D = 2.5\text{--}5.5$ by using finite volume method. Mean drag coefficient and average Nusselt number of U_C was usually higher than D_C , while for higher spacing ratios, change became insignificant. Ali *et al.* (2022a) investigated the forced convection on tandem cylinders at $Re = 100$ and varying $Ur = 2\text{--}14$ with two degree of freedom oscillating cylinders. Three different regimes were observed for varying spacing ratio $L/D = 1.5\text{--}6$: single body, reattachment, and co-shedding regime.

In the last few years, research on the effect of the corner radius of a square cylinder's FIV has been increased. Existing studies addressing the effect of corner radius of square cylinder's FIV is very limited. Most studies are confined to fixed cylinders with constant spacing ratio. In addition, coupling to forced convection was not investigated. The studies on different cross section, spacing ratio, mounting, and heat transfer are summarized in Table I, with key contribution of past researchers. Some of studies have adopted filleted radius along with forced convection although the effect of WIV (Wake Induced Vibration) and VIV has been omitted. To understand the flow characteristics and heat transfer, behaviors cannot be predicted on static cylinders. These features of configurations have not been explored in past. A systematic investigation is required on the effect of r^* and L/D on flow characteristics, aerodynamic forces, and heat transfer from oscillating filleted cylinders. In present work, the effect of corner radius has been studied for tandem square cylinders with a constant $Re = 150$ and varying Ur . Two different values of spacing ratio $L/D = 2$ and 4 have been analyzed to understand the physics of tandem cylinders from $r^* = 0$ (square cylinder) to 1 (circular cylinder). Both cylinders are maintained at constant wall temperature to examine heat transfer along with FIV.

II. MATHEMATICAL MODELLING

A. Model configuration and boundary assignments

Figure 1 shows the schematic diagram of computational domain and model configuration. Cylinders are positioned in tandem arrangement with center-to-center distance ($L = 2$ and 4), length $2R = D$ and

height $2R = D$ vertically centered in a large computational domain of width $S = 70D$ and height $H = 40D$ constituting a blockage ratio of 2.5% . Corners have rounded to generate the filleted geometry as $0 < r^* < 1$ for upstream and downstream cylinder. Both cylinders are allowed to vibrate in y direction independently due to hydrodynamic forces and constrained in x direction. Mass (m) is actual mass of cylinder, spring constant (k), and damping constant (c) govern the motion of cylinders. For heated cases, both cylinders are maintained at constant temperature $T^* = 1$ and free stream temperature at $T^* = 0$. Fluid enters the computational domain at constant density ρ , viscosity ν , free stream velocity U_∞ , and T_∞ . The Reynolds number of free stream is fixed at $Re = 150$.

B. Governing equations

The incompressible flow and heat transfer around a square cylinder is governed by conservation of mass, momentum, and energy, respectively, expressed mathematically as

$$\frac{\partial u}{\partial x} + \frac{\partial v}{\partial y} = 0, \quad (1)$$

$$\frac{\partial u}{\partial t} + u \frac{\partial u}{\partial x} + v \frac{\partial u}{\partial y} = -\frac{1}{\rho} \frac{\partial p}{\partial x} + \nu \left(\frac{\partial^2 u}{\partial x^2} + \frac{\partial^2 u}{\partial y^2} \right), \quad (2a)$$

$$\frac{\partial v}{\partial t} + u \frac{\partial v}{\partial x} + v \frac{\partial v}{\partial y} = -\frac{1}{\rho} \frac{\partial p}{\partial y} + \nu \left(\frac{\partial^2 v}{\partial x^2} + \frac{\partial^2 v}{\partial y^2} \right), \quad (2b)$$

$$\frac{\partial T}{\partial t} + u \frac{\partial T}{\partial x} + v \frac{\partial T}{\partial y} = \alpha \left(\frac{\partial^2 T}{\partial x^2} + \frac{\partial^2 T}{\partial y^2} \right), \quad (3)$$

where \vec{u} , p , and T are correspondingly velocity, pressure, and temperature. For the temperature range considered, fluid properties: density ρ , viscosity μ , specific heat capacity c_p , and thermal diffusivity α can be assumed constant. Buoyancy effects are not considered as this research work is proposed at $Ri = 0$, which is the ratio between buoyancy force and viscous forces. Gourari *et al.* (2019) stated buoyancy forces can be neglected at $Ri < 0.1$; hence, forced convection dominates in this region. Hence, gravity effect can also be neglected on the basis of Ri (Zafar and Alam, 2020). These governing equations are subjected to the initial conditions of $= 0$, $v = 0$, and $T = T_\infty$. The associated boundary conditions to the domain are the Dirichlet at the inlet ($u = U_\infty$, $v = 0$, $T = T_\infty$) and Neumann at the outlet ($\frac{\partial u}{\partial x} = \frac{\partial T}{\partial x} = 0$), no-slip and no penetration for upper and lower boundaries ($u = U_\infty$, $v = 0$, $T = T_\infty$), and the zero output pressure gradient ($p = p_{out}$). At the cylinder surfaces, no-slip and constant temperature $T^* = 1$ is enforced. At low Reynolds number of $Re = 150$ ($Re = \frac{2\rho U_\infty R}{\mu}$), the flow is reasonably two-dimensional. For the isothermal case and since the velocity of the flow is small below the Mach limit of 0.3 , the fluid indeed is incompressible and the energy equation is uncoupled and not involved. However, for the non-isothermal case, the energy became coupled, and hence, the density of the flow is followed with ideal gas and changes. In general term, the flow appears to be incompressible but with slight change in density specially near the cylinder surface this is not true. Generally, the Mach number is still very small to cause any shocking leading to shock wave formation and associated density or pressure jump. The flow is considered to be incompressible as density and viscosity are constant with temperature, and at

TABLE I. Summary of previous studies over different types of cross section with heat transfer.

Researchers	Method	Spacing ration	Cross section	Re	Mounting	Heat transfer	Contribution
Kumar and Sen (2021)	Num	5	Square	100	1 DOF–1 DOF	No	Effect of square cross section on VIV (Vortex Induced Vibration)
Khan <i>et al.</i> (2022)	Num	1.5, 3.5, and 5.5	Circular	100	1 DOF–1 DOF	No	Diameter ration and spacing ration dependence
Sun <i>et al.</i> (2021)	Num	4	Circular	150	1 DOF–1 DOF	Yes	Forced convection along with FIV
Zhang <i>et al.</i> (2019)	Num	1–8	Filletted	100	Fixed	Yes	Forced convection with rounded corners
Mittal and Kumar (2001)	Num	5.5	Circular	100	1 DOF–1 DOF	No	Beating phenomenon evolution with spacing ration
Zhu <i>et al.</i> (2019)	Num	2, 4, and 6	Circular/Prism	100	Fixed- 2 DOF	No	Different cross section at upstream changes shedding pattern
Mahir and Altaç (2008)	Num	2, 3, 4, 5, 7, and 10.	Circular	100 200	Fixed	Yes	Effect of spacing on heat transfer from cylinders
Nepali <i>et al.</i> (2020)	Num	5	Square	40–200	2 DOF–2 DOF	No	VIV of square with an effect of Re
Adeeb <i>et al.</i> (2018)	Num	1.5–10	Filletted	100	Fixed	No	Effect of corner and spacing ration combined
Borazjani and Sotiropoulos (2009)	Num	1, 2, 3	Circular	200	2 DOF–2 DOF	No	Proximity range explored
Lin <i>et al.</i> (2014)	Num	1.1–4	Circular	5–100	1 DOF–1 DOF	No	Asymmetric and symmetric regimes in FIV
Alam <i>et al.</i> (2003)	Exp	1–8	Circular	65000	Fixed	No	Fluctuating pressure distribution with spacing ratio
Alam <i>et al.</i> (2016)	Exp	4.6–6	Square	13000	Fixed	No	Staggered angle configuration
Bao <i>et al.</i> (2012)	Num	5	Circular	150	2 DOF–2 DOF	No	Varying natural frequency
Chen <i>et al.</i> (2018)	Num	1.2–5	Circular	100	1 DOF–1 DOF	No	Vibration response and galloping mechanism
Hu and Zhou (2008)	Exp	1.2–2	Circular	7000	Fixed	Yes	Staggered position with heat transfer
Huera-Huarte and Bearman (2011)	Exp	2–4	Circular	~12000	1 DOF–1 DOF	No	Frequency response of experimental vibrations
Mohany <i>et al.</i> (2014)	Exp	1.2–4.5	Circular	10000–300000	Fixed	No	Flow acoustic in turbulence regime
Dhiman <i>et al.</i> (2006)	Num	–	Square	1–45	Fixed	Yes	Effect of varying Re and Pr
Izadpanah <i>et al.</i> (2018)	Num	–	Circular	150	1-DOF	Yes	Varying Damping ratio along with heat transfer
Sarout <i>et al.</i> (2022a)	Num	–	Filletted	100–200	1 DOF	Yes	Corner radius with varying Re leads to higher heat transfer
Dwivedi and Dhiman (2019)	Num	2.5–5.5	Circular	100	Fixed	Yes	Thermal buoyancy with spacing ration

Re = 150, free stream velocity is relatively low to alter the flow properties (Dhiman *et al.*, 2006; Mittal *et al.*, 1997).

The upstream and downstream cylinders vibrate transversely under the action of various forces. The motion of the cylinders is governed by Newton's 2nd law of motion as

$$m \frac{d^2 Y}{dt^2} + c \frac{dY}{dt} + kY = F_y, \quad (4)$$

where Y is the y direction displacement of the square cylinder under the influence of the y direction hydrodynamic force per unit length (F_y).

The initial conditions imposed on the square cylinder are $Y = 0$ and $\frac{dY}{dt} = 0$.

The governing equations can be non-dimensionalized by introducing dimensionless parameters: $t^* = tU_\infty/(2R)$, $Y^* = Y/(2R)$, $\vec{u}^* = \vec{u}/U_\infty$, $\vec{u}^* = \vec{u}/U_\infty$, $p^* = p/\rho U_\infty^2$, and $T^* = (T - T_\infty)/(T_s - T_\infty)$. The dimensionless governing equations are

$$\frac{\partial u^*}{\partial x^*} + \frac{\partial v^*}{\partial y^*} = 0, \quad (5)$$

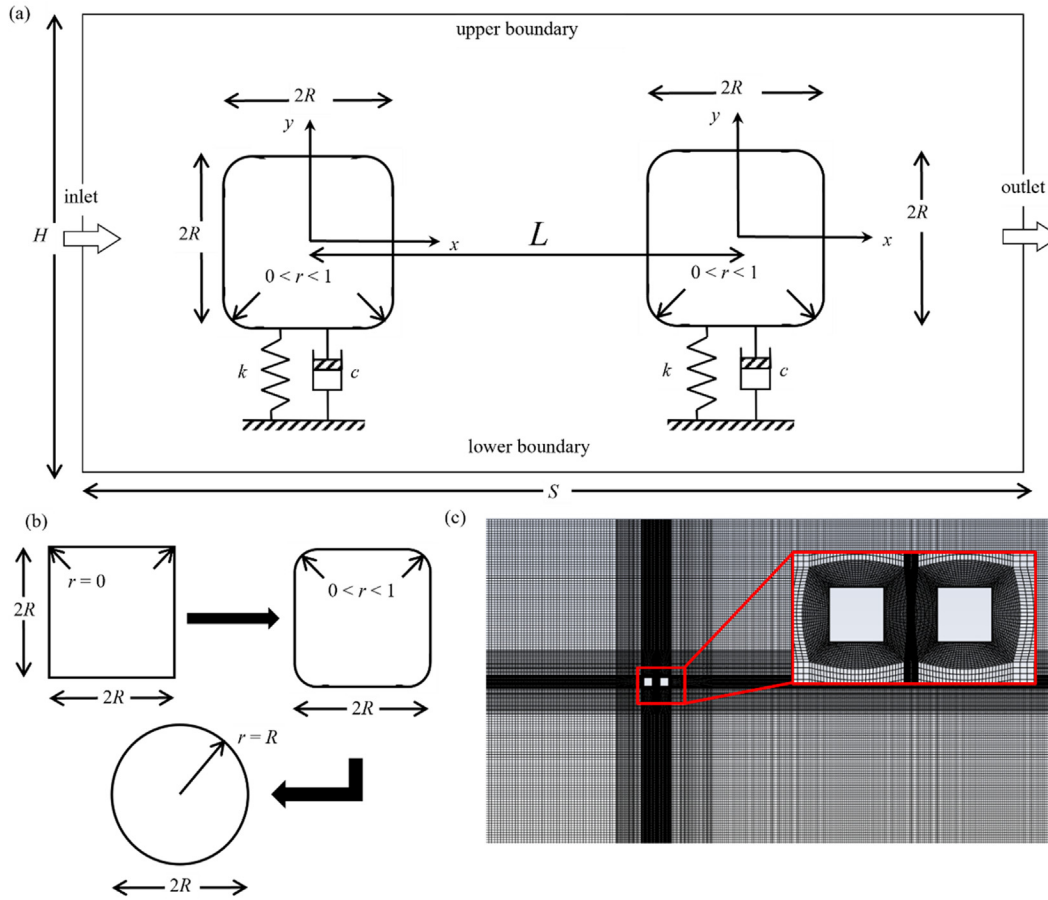


FIG. 1. (a) Computational domain containing two elastically supported tandem cylinders, (b) pictorial depiction of cylinder changing corner radius from square cylinder to circular cylinder with intermediate stages, and (c) meshing of computational domain with zoomed-in.

$$\frac{\partial u^*}{\partial t^*} + u^* \frac{\partial u^*}{\partial x^*} + v^* \frac{\partial u^*}{\partial y^*} = -\frac{\partial p^*}{\partial x^*} + \frac{1}{Re} \left(\frac{\partial^2 u^*}{\partial x^{*2}} + \frac{\partial^2 u^*}{\partial y^{*2}} \right), \quad (6a)$$

$$\frac{\partial v^*}{\partial t^*} + u^* \frac{\partial v^*}{\partial x^*} + v^* \frac{\partial v^*}{\partial y^*} = -\frac{\partial p^*}{\partial y^*} + \frac{1}{Re} \left(\frac{\partial^2 v^*}{\partial x^{*2}} + \frac{\partial^2 v^*}{\partial y^{*2}} \right), \quad (6b)$$

$$\frac{\partial T^*}{\partial t^*} + u^* \frac{\partial T^*}{\partial x^*} + v^* \frac{\partial T^*}{\partial y^*} = \frac{1}{Pr \cdot Re} \left(\frac{\partial^2 T^*}{\partial x^{*2}} + \frac{\partial^2 T^*}{\partial y^{*2}} \right), \quad (7)$$

$$\frac{d^2 Y^*}{dt^{*2}} + 4\pi F_n \zeta \frac{dY^*}{dt^*} + (2\pi F_n)^2 Y^* = \frac{2C_L}{\pi m^*}, \quad (8)$$

where the dimensionless parameters are the reduced velocity $Ur = \frac{U_\infty}{f_n D}$, the Reynolds number $Re = \frac{2\rho U_\infty R}{\mu}$, the Prandtl number $Pr = \frac{c_p \mu}{k}$, damping ratio $\zeta = \frac{c}{m f_n}$, mass ratio $m^* = \frac{Mass_{cylinder}}{\rho \cdot Volume_{cylinder}} : r^* = 1; \frac{4m}{\pi \rho (2R)^2}$, normalized natural frequency $F_n = \frac{2R f_n}{U_\infty}$, and undamped natural frequency $f_n = \frac{1}{2\pi} \sqrt{\frac{k}{m}}$.

The instantaneous drag and lift coefficients C_D and C_L are defined, respectively, from the drag force F_x and lift force F_y as

$$C_D = \frac{F_x}{\frac{1}{2} \rho U_\infty^2 (2R)}, \quad (9)$$

$$C_L = \frac{F_y}{\frac{1}{2} \rho U_\infty^2 (2R)}. \quad (10)$$

These are integrated to obtain the average drag and lift coefficients as

$$\overline{C_D} = \frac{\sum_{i=1}^N C_D(i)}{N}, \quad (11)$$

$$\overline{C_L} = \frac{\sum_{i=1}^N C_L(i)}{N}. \quad (12)$$

C. Solution procedure

The governing equations for the discretized flow domain subjected to appropriate flow conditions were solved using Ansys Fluent, which is a finite volume-based solver. The transient, convective, and diffusive terms are discretized, respectively, first-order implicit and second-order central schemes. Equation (8) governing the oscillatory motion of the square cylinder integrated using fourth-order

Runge–Kutta method implemented via a user-defined function (UDF) within Ansys Fluent environment. The unsteady solution was sought for the fluid subjected to incoming velocity and temperature, and the initial cylinder was positioned within the dynamic mesh region. The hydrodynamic forces were computed at each time step. The net y-direction hydrodynamic force was evaluated to determine the cylinder displacement and velocity at that instant time step (Sen and Mittal, 2011; Willden and Graham, 2006). The cylinder displacement was used to adjust the cylinder to the new position, while the velocity was accounted as the no-slip cylinder surface velocity in the successive time step solution of the fluid equations [Eqs. (5)–(7)]. The time advancement was continued by the above process until a quasi-steady/periodic response was achieved. The Courant–Friedrichs–Lewy (CFL) number is 0.5 for the entire computational domain (Kumar and Sen, 2021). For setting the convergence criterion, residual value sets to be $1e-6$ for continuity, x-velocity, y-velocity, and energy.

D. Mesh sensitivity and validation

Three different meshes with the same O-grid type meshing scheme and finer mesh near the cylinder's surfaces are implemented. Crucial parameters such as vibration amplitude A/D , average drag coefficient $\overline{C_D}$, and average Nusselt number Nu_{avg} are tabulated in Table II. Mesh-I, II, III, and IV have, respectively, 10 344, 50 234, 72 453, and 80 234 nodes. The difference in the results obtained from Mesh II (baseline), and the finer Mesh III is small. The time increment leading to the spatial resolution is kept at $\Delta t^* = 0.01$, and solutions obtained from Mesh II are mesh independent and will be used in the subsequent study (with slight modifications to accommodate the cylinders' filleted corners).

Percentage errors show the deviation of generated values from Sun et al. (2021). The present predictions [Fig. 2(b)] at $Re = 150$, $m^* = 2$, and $Ur = 10$ are compared and in close agreement with those of Sun et al. (2021). Standard deviation from the actual values has been plotted in Fig. 2(a). The highest uncertainty can be observed in the case of vibrational amplitude, and it depends on the mesh refinement, time step, and iteration per time step. Mesh sensitivity brings robustness to the numerical simulations and can predict the uncertainties in FIV (Wang et al., 2018).

III. RESULTS AND DISCUSSION

Both cylinders are elastically supported with $m^* = 10$, and r^* is changed from 0 (square) to 1 (circular cylinder). For higher amplitude,

the structural damping constant is set to be zero (ξ). Forced convection is carried out over the cylinders at a constant $Re = 150$ and $Pr = 0.7$. Reduced velocity (Ur) is varied from 2 to 10 by changing the value of spring constant k . Two spacing ratios (L/D) = 2 and 4 are investigated for the detailed analysis of flow separation, recirculation behind cylinder, and vortex shedding with three distinctive flow regimes. The effect of r^* on flow characteristics is demonstrated by vibration amplitudes, flow contours, streamlines, f_s/f_n frequency response, and phase diagrams.

A. Flow topology for $L/D = 4$

Figure 3 shows the effect of corner radii with changes on aerodynamics and heat transfer parameter. A pattern can be observed for all values of A/D in Fig. 3(a); that is, there is the minimal vibrational amplitude at lower values at $r^* = 1$ and 0.75 for low Ur . At $Ur = 6$, for $r^* = 1$ and 0.75, maxima is achieved for U_C and D_C (Khan et al., 2022). Vibrational amplitude of D_C is higher than U_C for both of these cases. An interesting phenomenon observed for $r^* = 0$ and 0.5 between $Ur = 6 \sim 8$. Maximum values of A/D have shifted from $Ur = 6$ to $Ur = 8$ for $r^* = 0$ and 0.5 (Zhao and Zhao, 2019). From the graph, it is observed that for a particular Ur , the vibrational amplitude reaches to its maximum value and after it dips to a lower value. A generalized assertion can be deduced that rigorous vibration occurs in downstream cylinder as compared to upstream cylinder. This phenomenon is known as wake-induced vibration (Bao et al., 2012).

Figure 3(c) shows the $\overline{C_D}$ variation with Ur for different corner radii. Highest $\overline{C_D}$ is observed for square cylinder and having bigger wake at rear of the U_C . For D_C , lower Ur generates negative value of average drag coefficient ($\overline{C_D}$) as cylinders are not oscillating (Adeeb et al., 2018). There is a low-pressure region behind the upstream cylinder, which generates a suction for downstream cylinder. A net force is generated from right to left on downstream cylinder, as the low-pressure region behind the downstream cylinder has lower vibrational amplitude as compared to upstream cylinder. For $r^* = 0-1$ & $Ur = 2 \sim 4$, there is huge difference in $\overline{C_D}$ for U_C and D_C . As Ur increases from 4 to 6, lock-in occurs for $r^* = 0.75$ and 1 causing U_C to vibrate at a certain amplitude. As the vortex sheds from the U_C hits D_C causing it to vibrate more rapidly than D_C . A sudden peak in the value of $\overline{C_D}$ for D_C can be noticed. Due to the shape change, lock-in for $r^* = 0$ and 0.5 occurs around $Ur = 8$, a sharp change can be seen in $\overline{C_D}$ from $Ur = 6$ to $Ur = 8$ for downstream cylinder. The fluctuation of downstream

TABLE II. Numerical simulation results for $Re = 150$, $m^* = 2$, and $Ur = 10$. FIV parameters such as maximum amplitude, average drag coefficient, and Nusselt Number are summarized.

Mesh	Nodes	$A/D(U_C)$	$A/D(D_C)$	$\overline{C_D}(U_C)$	$\overline{C_D}(D_C)$	$Nu_{avg}(U_C)$	$Nu_{avg}(D_C)$
Mesh-I (coarse)	10 344	0.113	0.619	1.102	1.067	5.424	9.359
Error percentage		12.1%	4.29%	4.29%	5.65%	6.78%	5.93%
Mesh-II (baseline)	50 234	0.125	0.647	1.150	1.096	5.611	9.632
Error percentage		3.0%	2.8%	5.66%	3.09%	3.57%	3.18%
Mesh-III (fine-I)	72 453	0.127	0.648	1.170	1.125	5.712	9.723
Error percentage		1.55%	0.14%	4.01%	0.53%	1.8%	2.27%
Mesh-IV (fine-II)	80 234	0.127	0.648	1.170	1.125	5.712	9.723
Error percentage		1.55%	0.14%	4.01%	0.53%	1.8%	2.27%
Sun et al. (2021)	15 999	0.129	0.6490	1.219	1.131	5.819	9.949

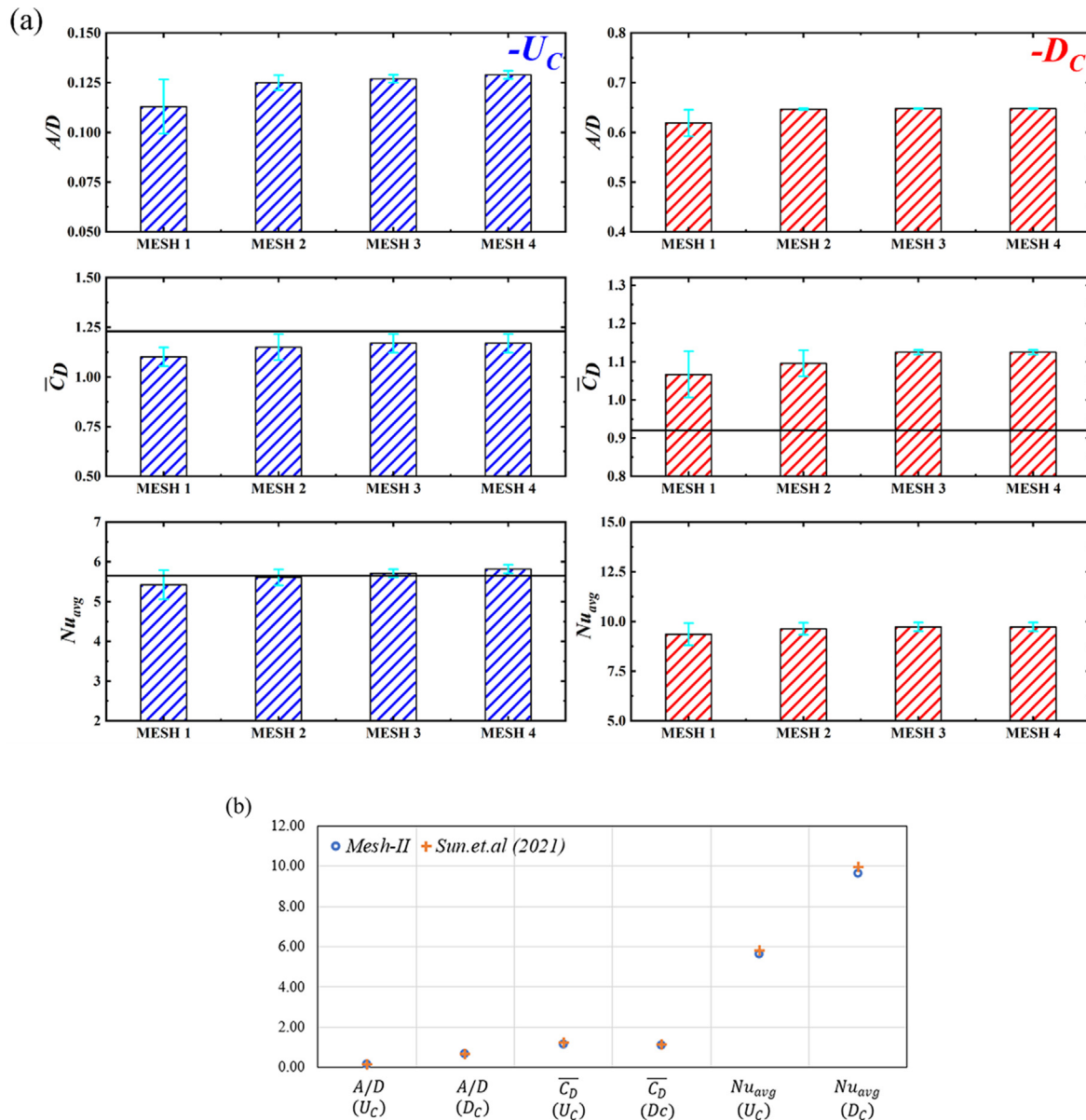


FIG. 2. (a) Standard deviation for the computational measurement for four different mesh sizes at various parameters. (b) Comparison of results with published results of Sun et al. (2021) at for $Re = 150$, $m^* = 2$, and $Ur = 10$.

cylinder's $\overline{C_D}$ is more due to the function of upstream wake (Alam et al., 2003).

Figure 3(b) shows the effect of r^* on C_L with varying reduced velocity. Vibrational amplitude and C_L are correlated, and the effect of it can be seen in given plots. At $Ur = 2 \sim 4$, there is a very minimal coefficient of lift for $r^* = 0-1$ except some of the cases. Downstream cylinder of $r^* = 0$ and 1 has higher C_L as both cases acting as a single body (reattachment) with weak vortex shedding past downstream cylinder. At $Ur = 6$, for $r^* = 0.75$ and 1, vibrational amplitude A/D and lift coefficient C_L shoot up as lock-in occurs. C_L is higher for the

downstream cylinder because vortex sheds from the U_C impinge on the front surface of the D_C . $r^* = 0.75$ breaks the steady flow regime to enter in unsteady flow.

Figure 4 shows different Z-vorticity contours for all the defined cases at different Ur . Detachment of shear layer followed by rolling of those shear layer due to wake behind the cylinder causes vortex shedding. For square cylinders at $Ur = 2 \sim 6$, the shear layer separated from U_C gets reattached to D_C causing it to behave like a single cylinder with unsteady flow (Yao and Jaiman, 2019). Separation occurs from leading edge of U_C attached again to leading edge of D_C .

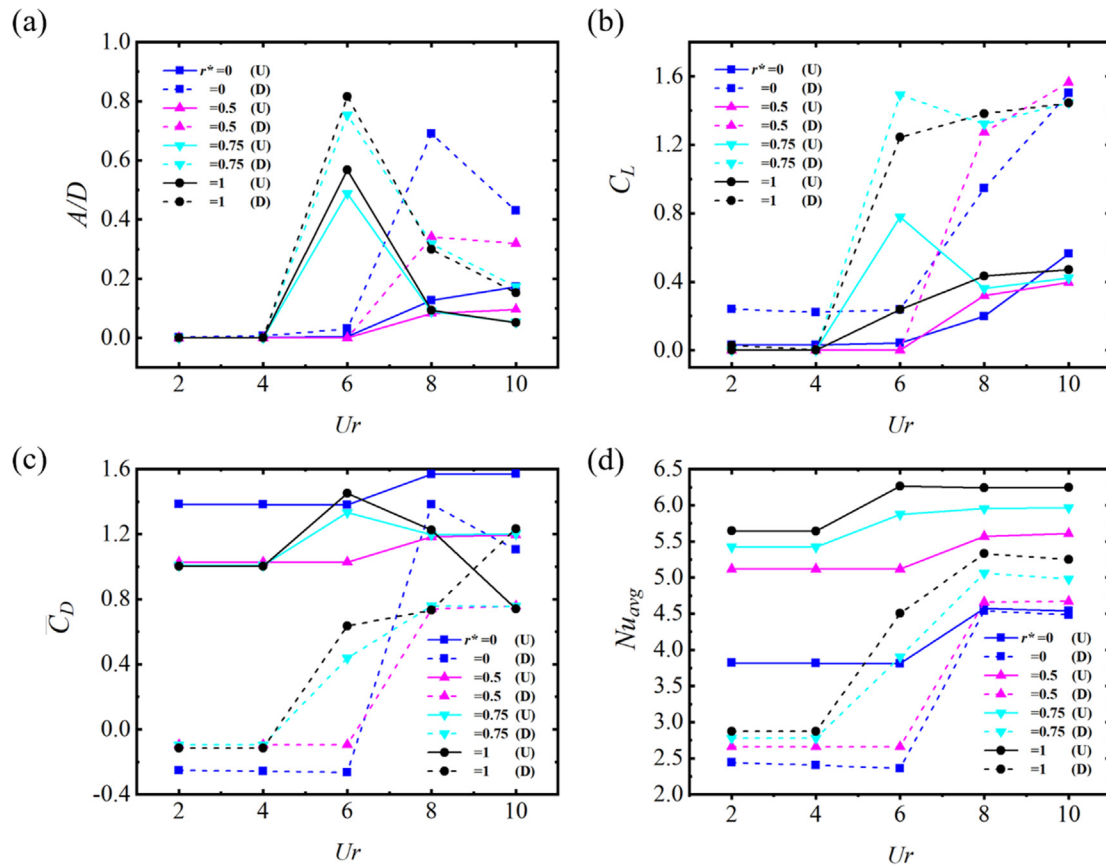


FIG. 3. Effect of r^* on FIV of the tandem cylinder for $L/D = 4$ by varying Ur (a) A/D vs Ur , (b) C_L vs Ur , (c) $\overline{C_D}$ vs Ur , and (d) Nu_{avg} vs Ur .

Two square cylinders are not vortices in alternate manner with inline formation. This exhibits the 2S vortex shedding from two cylinders together. For $Ur = 8$ and $r^* = 0$, shear layers are pushed into two parallel streets by the vibration of downstream cylinder causing C(2S) past D_C .

Figure 5 shows the streamlined structure of wakes behind the cylinders. Streamlines for square cylinder show a varying wake for all reduced velocities behind the U_C . For a square cylinder, at higher Ur , wake behind the U_C becomes significantly low as vortices from U_C start dominating the region. Even in reattachment regime, there are some distinctions. As it can be observed for $r^* = 0.5$ and 0.75 at $Ur = 2 \sim 6$, flow getting separated at the trailing edge of the U_C and getting reattached at D_C . Steady flow can be observed past downstream cylinder. As shown in Fig. 5, wake at $r^* = 0.5$ at $Ur = 6$ is symmetrical for both U_C and D_C .

Flow characteristics of this set are similar to the steady flow past an isolated cylinder. No vortex shedding is observed past downstream cylinder. Flow topology becomes different at $r^* = 0.75$, and higher vibrational amplitude of D_C becomes massively high. In the case of circular cylinder, tandem cylinders at $Ur = 2$ and 4 act as single cylinders due to reattachment, and 2S vortex shedding can be observed for the $Ur = 2$. $r^* = 1$ and $Ur = 4$ vortices from the upper surface of cylinder and lower surface of D_C . A major similarity is observed for $r^* = 0$ and

1 at $Ur = 2$, and wake structure is changing behind upstream cylinder, but no actual presence of wake is observed at the downstream cylinder.

For $r^* = 1$ and $Ur = 6$, physics of flow becomes more dynamic as the cylinder is their peak of vibrational amplitude as shown in Fig. 3(a). Vortices from U_C are impinging on the D_C periodically, and vortices from upper surface of U_C interact with separation at the lower surface of D_C . This interaction causes vortex stretching nearby the downstream cylinder and lies under “co-shedding” (Griffith *et al.*, 2017). Vortex shedding from tandem cylinders changes to 2S or Von Karman vortex shedding. As Ur reaches the threshold of 6, unsteady flow starting to emerge for $r^* = 0.75$ and 1 similarly results started showing up for $r^* = 0$ and 0.5 at $Ur = 8$. For square cylinder past $Ur = 8$, unsteady flow is actively present. As shown in Fig. 4, vortex shedding from cylinders start as 2S, and in later stages, it turns to be C(2S). There is reasonable gap in vortices as D_C is currently under lock-in period. For $r^* = 0.5$, it does occur at $Ur = 8$, as compared to square cylinder vortex shedding amplitude, which is significantly low. This causes vortices to shed in an inline manner, and vortices are formed in combination of C(2S) and 2S. A sharp drop is observed for all cases after the lock-in period. Most of the cases from $r^* = 0.5 \sim 1$ at $Ur = 8 \sim 10$ shows similar flow structure behind the D_C .

Figure 6 shows the instantaneous velocity and pressure contours for $r^* = 0-1$. In the case of square cylinder at $Ur = 6$, there is a

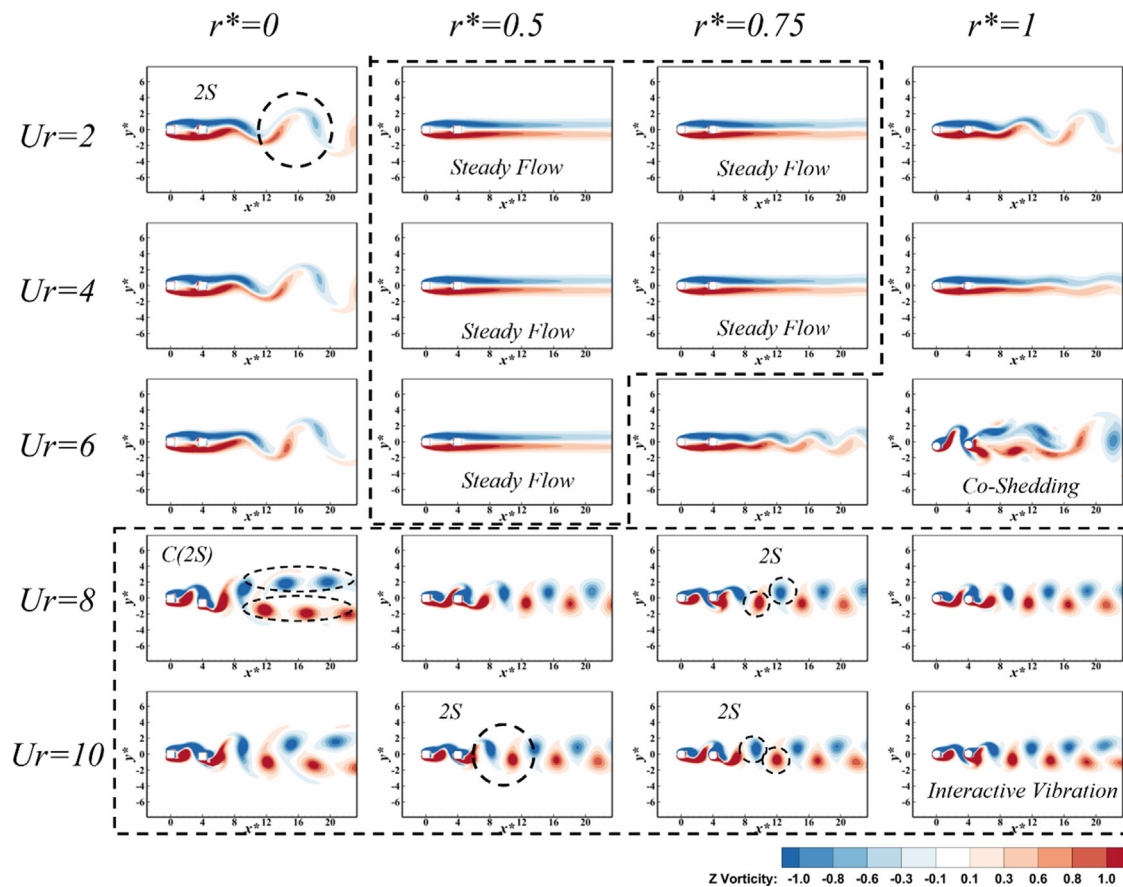


FIG. 4. Z-vorticity contours for varying $r^* = 0-1$ and $Ur = 2-10$ for $L/D = 4$.

prominent low pressure between the cylinder, which can be confirmed by negative value of $\overline{C_D}$. As fluctuation starts in upstream cylinder causes a varying low-pressure region between the cylinders and past downstream cylinder another fluctuating wake can be observed which is similar to Yao and Jaiman (2019). Although when U_C and D_C both vibrate, it causes a larger wake as compared to other cases. This difference is prominent in $Ur = 6$ and $Ur = 8$ for $r^* = 0$. Other configurations are similar in nature, but values fluctuate on the bases of type of vibration as in the case of $Ur = 6$ for $r^* = 0.5$ and 0.75 , and velocity and streamlines show that steady flow does not fluctuate more as compared to crossheading. Although for circular cylinder at $Ur = 6$, co-shedding phenomenon is taking place; hence, a huge wake is formed behind the downstream cylinder.

Vortex shedding imprints are captured by contours of f_s/f_n and power spectral density of lift coefficient for $L/D = 4$. Figure 7 shows the ratio of natural frequency and vortex shedding frequency as dotted line shows the lock-in period where $f_n/f_s = 1$. From the Figs. 3(a) and 7(a), it is evident that lock-in for U_C and D_C occurs at $Ur = 6$ (Williamson, 1996). Synchronization remained persisted at the same values of Ur for $r^* = 0.75$. As corner radii started to decrease, there is shift start occurring for $r^* = 0.75$ and 1 as dotted line tilts toward the $Ur = 8$. Downstream cylinders try to resist the “shift,” but fluctuation in U_C will cause changes in D_C .

Figures 8(a)–8(d) illustrate the shedding frequency for $r^* = 0-1$ at $Ur = 6$. Shedding frequency of $r^* = 0$ is less than the natural frequency ($f_n = 0.166$). $r^* = 0.5$ generates identical results as $r^* = 0$. Values of downstream cylinder and upstream cylinder frequency are almost identical. Shedding frequency at $r^* = 1$ and 0.75 escalates quickly to higher values. f^* for $r^* = 1$ and 0.75 approaching the natural frequency ($f_n = 0.166$). A second peak is observed for $r^* = 1$ and $r^* = 0.75$ illustrating frequency modulation (f_{mod}). Figures 8(e)–8(h) depict the shedding frequency at $Ur = 8$ for $r^* = 0-1$. $r^* = 0$ (square cylinder) and $r^* = 0.75$ registered the growth in f^* while changing the reduced velocity. Primary vortex shedding approaches the natural frequency ($f_n = 0.125$) with the modulation. At $r^* = 0$, change in vortex shedding for D_C is higher as compared to U_C (Borazjani and Sotiropoulos, 2009; Prasanth and Mittal, 2009). Vortex shedding frequency of $r^* = 0.75$ and $r^* = 1$ (D_C/U_C) has surpassed the natural frequency ($f_n = 0.125$). Frequency modulation has been omitted from circular cylinder at $Ur = 8$. From Fig. 8, conclusion can be drawn on the lock-in phenomenon as lock-in for $r^* = 0$ and 0.5 occurs as $Ur = 8$, while for $r^* = 0.75$ and 1 occurs as $Ur = 6$, respectively.

Figure 9 shows phase diagrams for different corner radii at three Ur for U_C and D_C . At $Ur = 4$, for all cases C_L and Y^* appear to be in same phase. At $Ur = 6$, lock-in occurs, which is also shown in the

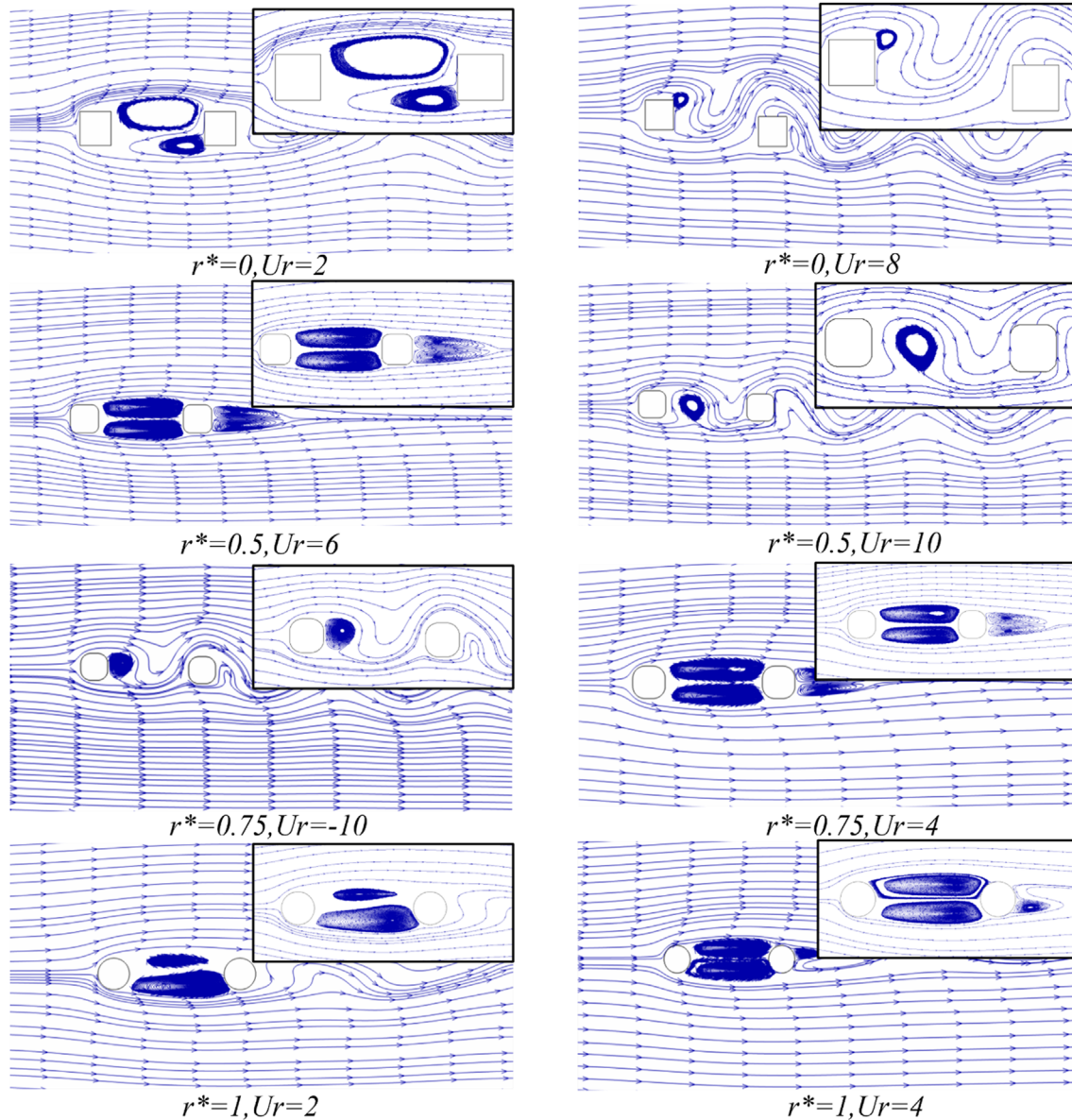


FIG. 5. Velocity streamlines for different cases showcasing variants of wake behind the cylinders.

graphs of U_C and D_C at $r^* = 0.75$ and 1. For $r^* = 1$ and 0.75, phase lag can be observed at $Ur = 8$.

Amplitude for upstream and downstream cylinder has dropped to a certain lower value contrary to the nature of C_L , which is stringent to higher values. For all cases with U_C and D_C , phase change is occurred when Ur changes from 6 to 8 (Lin et al., 2014). Equation (13) will provide the direction of force, which dictates the position of cylinder

$$\frac{F_Y}{kY} = 1 - \left(\frac{f_s}{f_n} \right)^2. \quad (13)$$

Figures 10(a)–10(d) show the dependence of Nu on θ for $Ur = 6$ at $r^* = 0$ –1. For square cylinder, the frontal area has higher Nu

because frontal area is in direct contact of upcoming flow. At $\theta = 45^\circ$, it depicts rise for Nu due to sharp edge. Heat transfer after 45° started dropping due to side bubble for $r^* = 0$. Low Nu at the frontal part of D_C ($r^* = 0$) due to the presence of “dead water” between the cylinders. At $r^* = 0.75$, a smooth curved is followed as started from lower to higher Nu at corner of geometry. Nu dropped to lower values after $\theta = 135^\circ$ due to shear layer separation, which reattached to downstream cylinder around $\theta = 35^\circ - 45^\circ$. As shown in Fig. 10, separation from downstream cylinder is almost at the same angle as upstream as separation is dependent on the geometry.

Almost same characteristics are shown by $r^* = 0.5$ and $r^* = 0.75$, as only flow separation angle has been shifted from 135° to 120° .

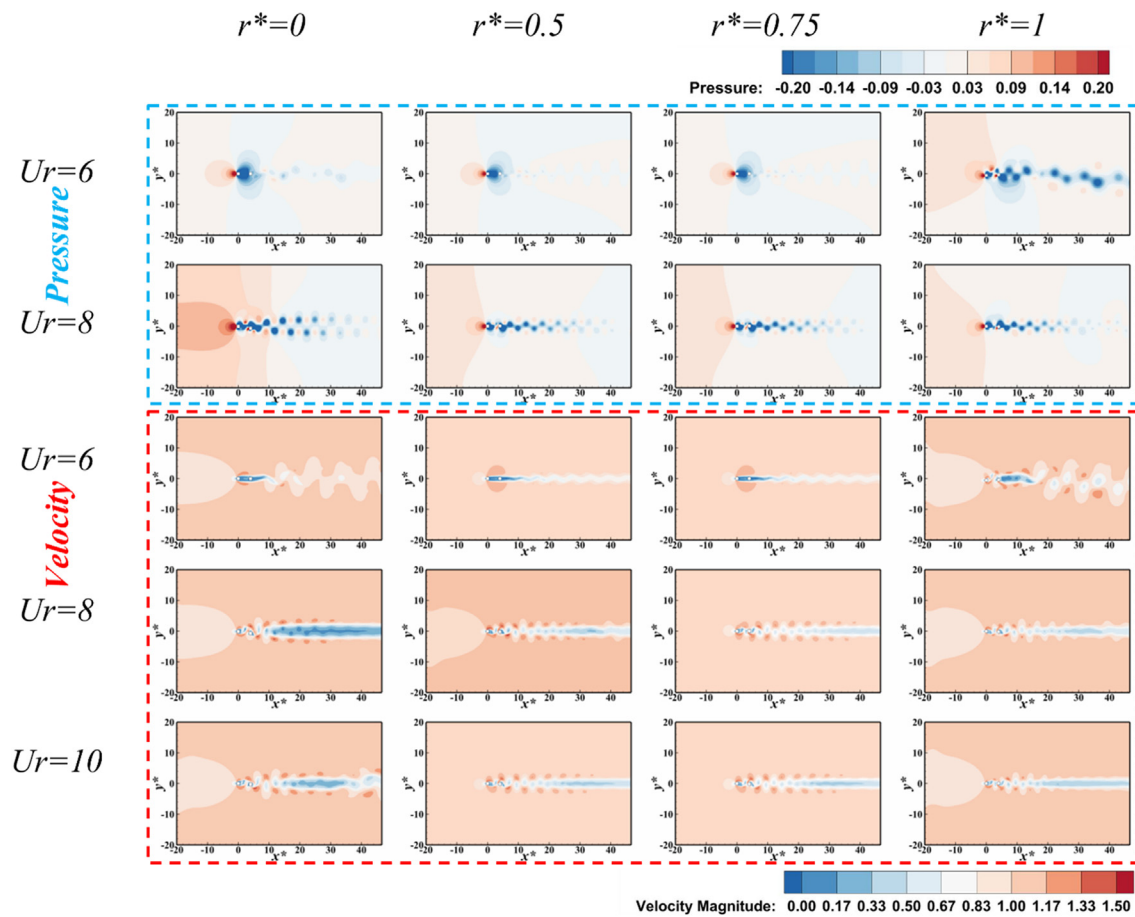


FIG. 6. Instantaneous contours plots of pressure marked in cyan for $r^* = 0-1$ at $Ur = 6$ and 8 with velocity contours marked in red for $r^* = 0-1$ at $Ur = 6, 8$, and 10 with spacing $L/D = 4$.

For circular cylinder, a perfect curve is followed as 0° have highest Nu . Along the circular cylinder, sudden drop can be observed in Nu for circular cylinder indicating flow separation due to adverse pressure gradient. Separation angle for U_C is around 125° , while for D_C , it is at 135° .

Figures 10(e)–10(h) depict the polar graph between Nu and θ for $Ur = 8$ at $r^* = 1$. The purpose of illustrating polar graphs at two different reduced velocities is to understand the effect of vibrational amplitude at transitional level. For $r^* = 0$, $Nu(D_C)$ have increased

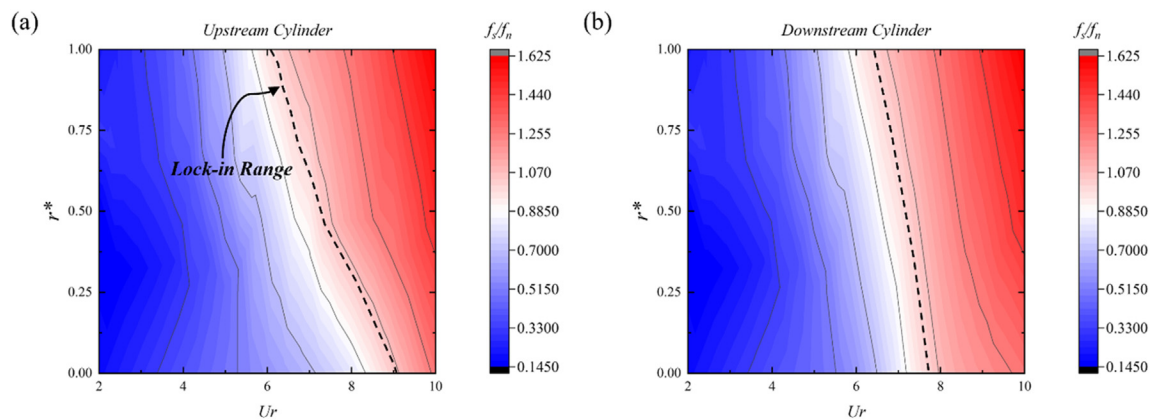


FIG. 7. Contours of f_s/f_n frequency response at $L/D = 4$ of (a) Upstream cylinder and (b) downstream cylinder with varying r^* and Ur .

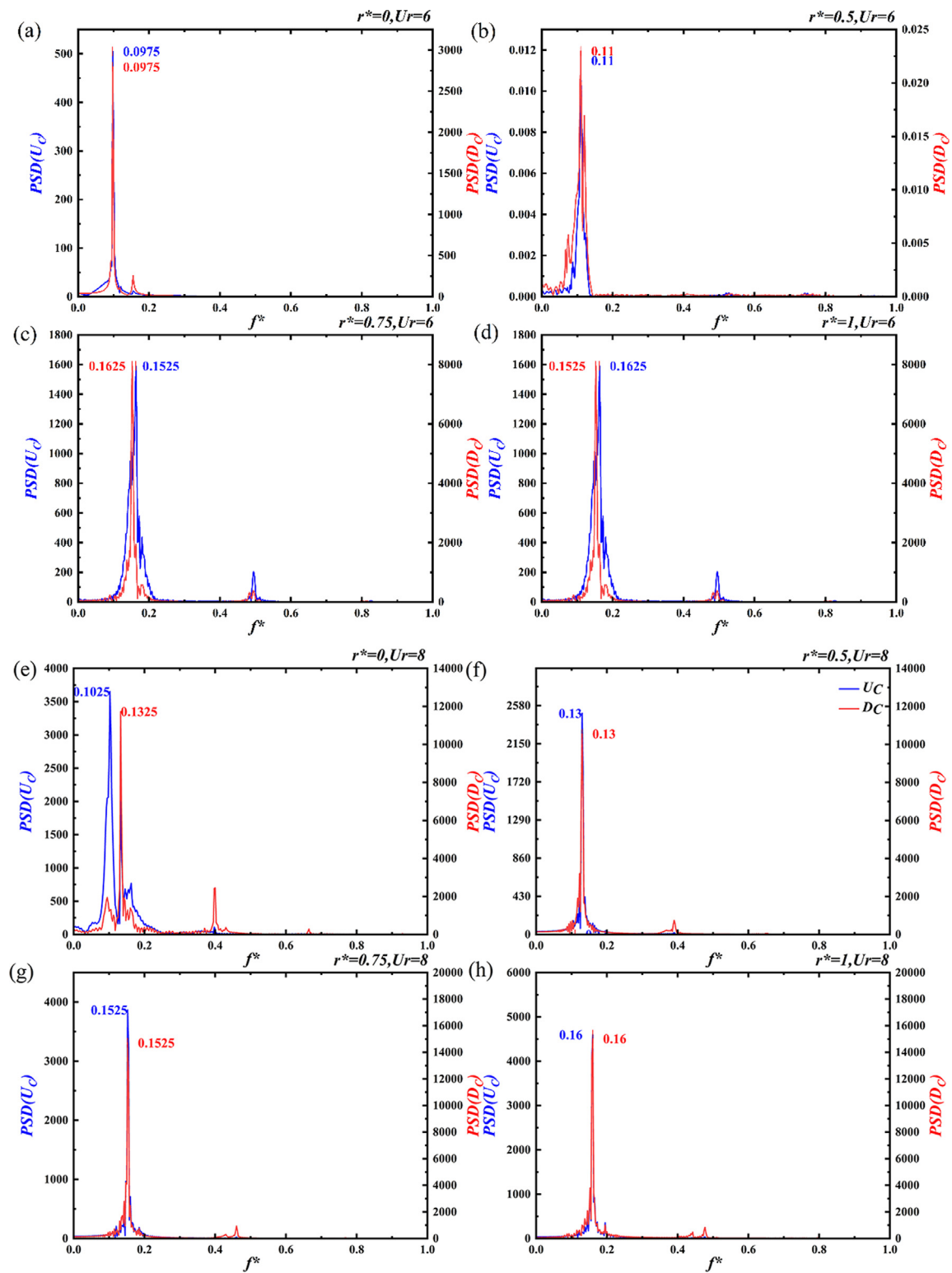
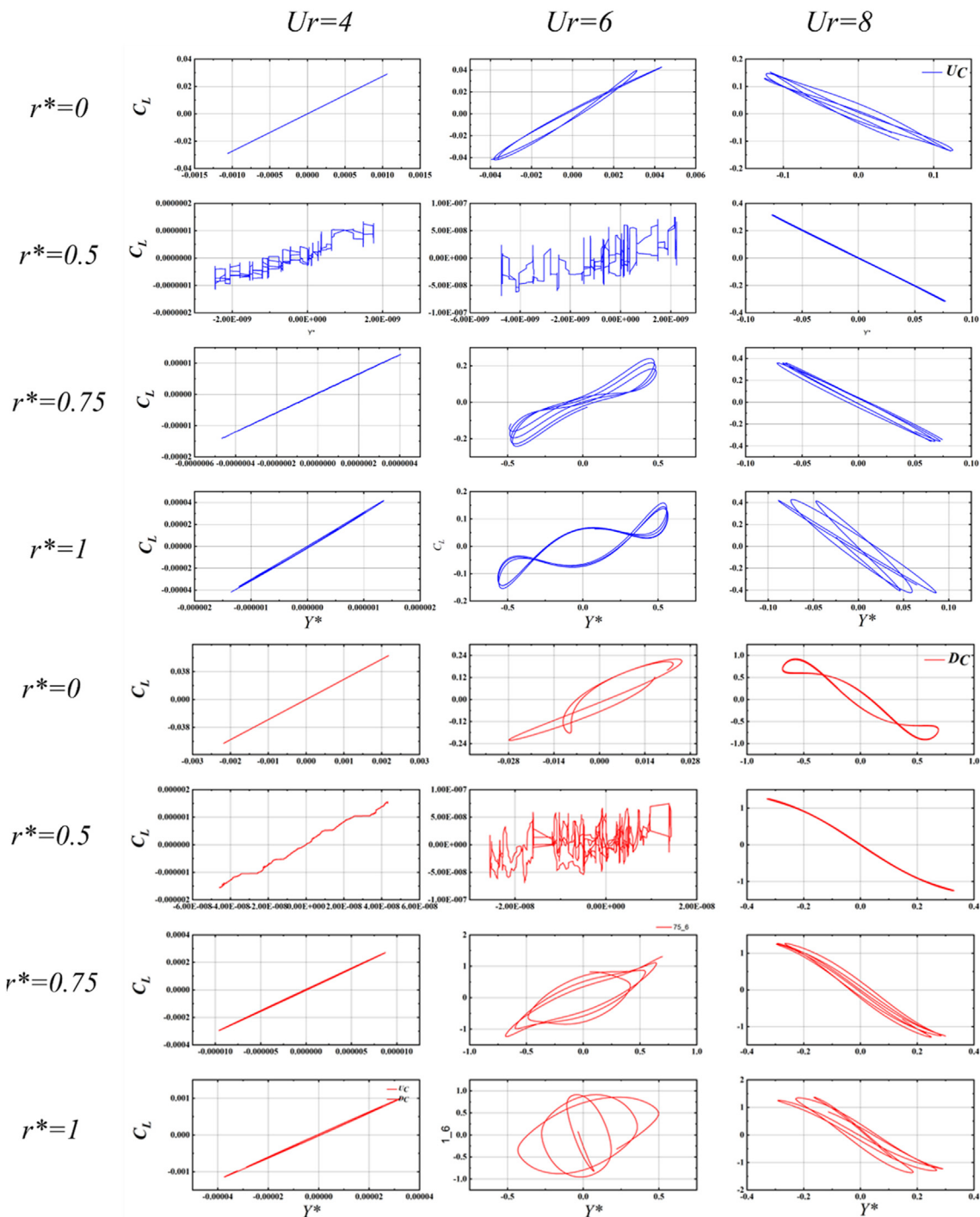


FIG. 8. Power spectral density of lift coefficient for $L/D = 4$ at reduced velocity $Ur = 6$ and 8 , (a)–(e) $r^* = 0$ (square cylinder), (b)–(f) $r^* = 0.5$, (c)–(g) $r^* = 0.75$, and (d)–(h) $r^* = 1$ (circular cylinder).


 FIG. 9. Phase diagram of upstream cylinder (blue grid) and downstream cylinder (red grid) at $Ur = 2, 4$, and 8 .

due to vibrational amplitude although position of point of separation has not changed. Core of $r^* = 0.5$ and $r^* = 0.75$ for downstream cylinder has changed as downstream, which has shown vibration. At $Ur = 6$ and $r^* = 0.75$ have sufficient but downstream cylinder is in

movement synchronization with upstream cylinder. For circular cylinder at $Ur = 8$, vibrations have suppressed for upstream cylinder in contrast to downstream, which leads to the interaction of shear layers from U_C with D_C .

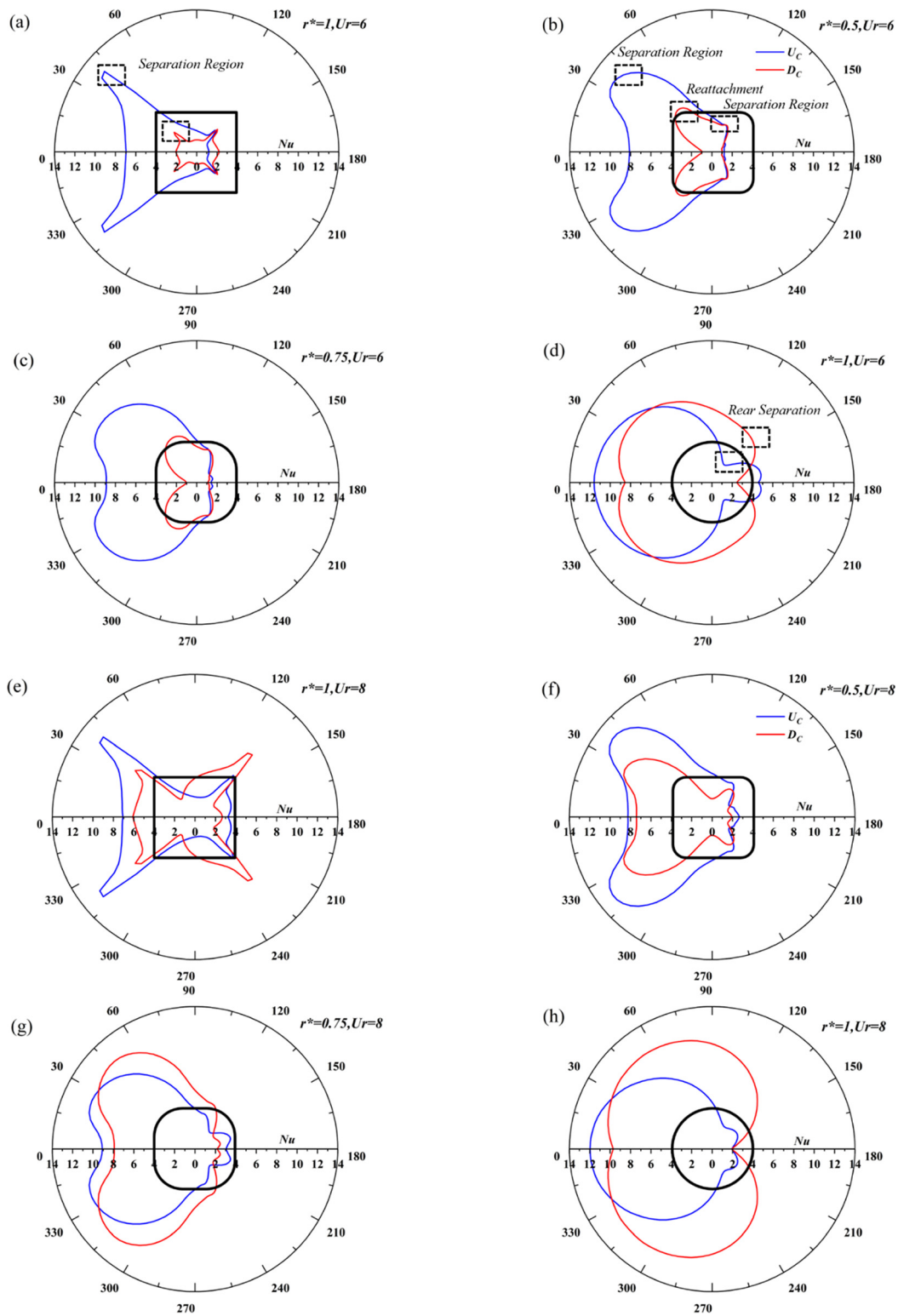


FIG. 10. Dependence on θ point averaged Nusselt number Nu for $L/D = 4$ at reduced velocity $Ur = 6$ and 8 , (a)–(e) $r^* = 0$ (square cylinder), (b)–(f) $r^* = 0.5$, (c)–(g) $r^* = 0.75$, and (d)–(h) $r^* = 1$ (circular cylinder).

Figure 11 shows the non-dimensional temperature variation around the cylinder when it is maintained at a constant temperature. Upcoming flow at $T^* = 0$, $Re = 150$, and $Pr = 0.7$ and cylinders' surface are maintained at $T^* = 1$. White color ($T^* = 0$) in domain signifies the presence of unaffected area from heat transfer around the cylinder. Nu_{avg} of downstream cylinder is highly dependent on the Nu_{avg} of upstream cylinder (Alam *et al.*, 2021; 2020). Overall, Nu_{avg} is dependent on flow topology and vibrational amplitude. Higher vibrational amplitude led to the higher Nu_{avg} . Figure 3(d) shows the Nusselt number dependence on Ur and r^* . In the case of square cylinder, Nu_{avg} is relatively low as compared to other cases; at $r^* = 0$, flow separation occurs at the trailing edge of square cylinder, which is early separation that causes poor heat transfer (Dhiman *et al.*, 2006). Heated flow from the upstream cylinder reattaches to downstream cylinder, causing poor heat transfer from D_C for $Ur = 2 \sim 4$ (Zhou and Yiu, 2006). Even for D_C , delayed flow separation causes better heat transfer (Dwivedi and Dhiman, 2019).

As soon as cylinder reaches in lock-in period, a rise can be seen in Nu_{avg} for U_C and D_C . The rise in D_C is more evident and sharper because D_C is getting exposed to fresh flow, which led to better heat

transfer. At $r^* = 0.75 \sim 1$ for $Ur = 6$ and $r^* = 0.75 \sim 1$ for $Ur = 8$ and, a sharp change in Nu_{avg} can be observed for D_C . Same shift can be observed in the value of Nu_{avg} . Vibrational amplitude of D_C at $r^* = 0$ at $Ur = 8$ is significantly higher than $r^* = 0.50$ at $Ur = 8$, but Nu_{avg} of $r^* = 0$ is slightly lower than $r^* = 0.50$ at $Ur = 8$. This defines the flow topology over the downstream cylinder and defies the completed dependence of Nu_{avg} at A/D (Sun *et al.*, 2021).

B. Flow topology for $L/D = 2$

Figure 12 shows corner radii effect on the FIV and heat transfer parameters at $L/D = 2$. A general trend can be observed for the upstream and downstream cylinder in Fig. 12(a); that is, a very low vibrational amplitude is observed at $Ur = 2 \sim 4$ for $r^* = 0 \sim 1$. As enormous rise in A/D can be seen for U_C and D_C at $r^* = 1$, vortex shedding frequency approaches the vortex shedding frequency (Khalak and Williamson, 1997).

At $Ur = 6$, maximum value of U_C and D_C is achieved for circular cylinder. A significant change has been observed in $r^* = 0.5$ and 0.75 as vortices from U_C start hitting D_C , although due to less spacing

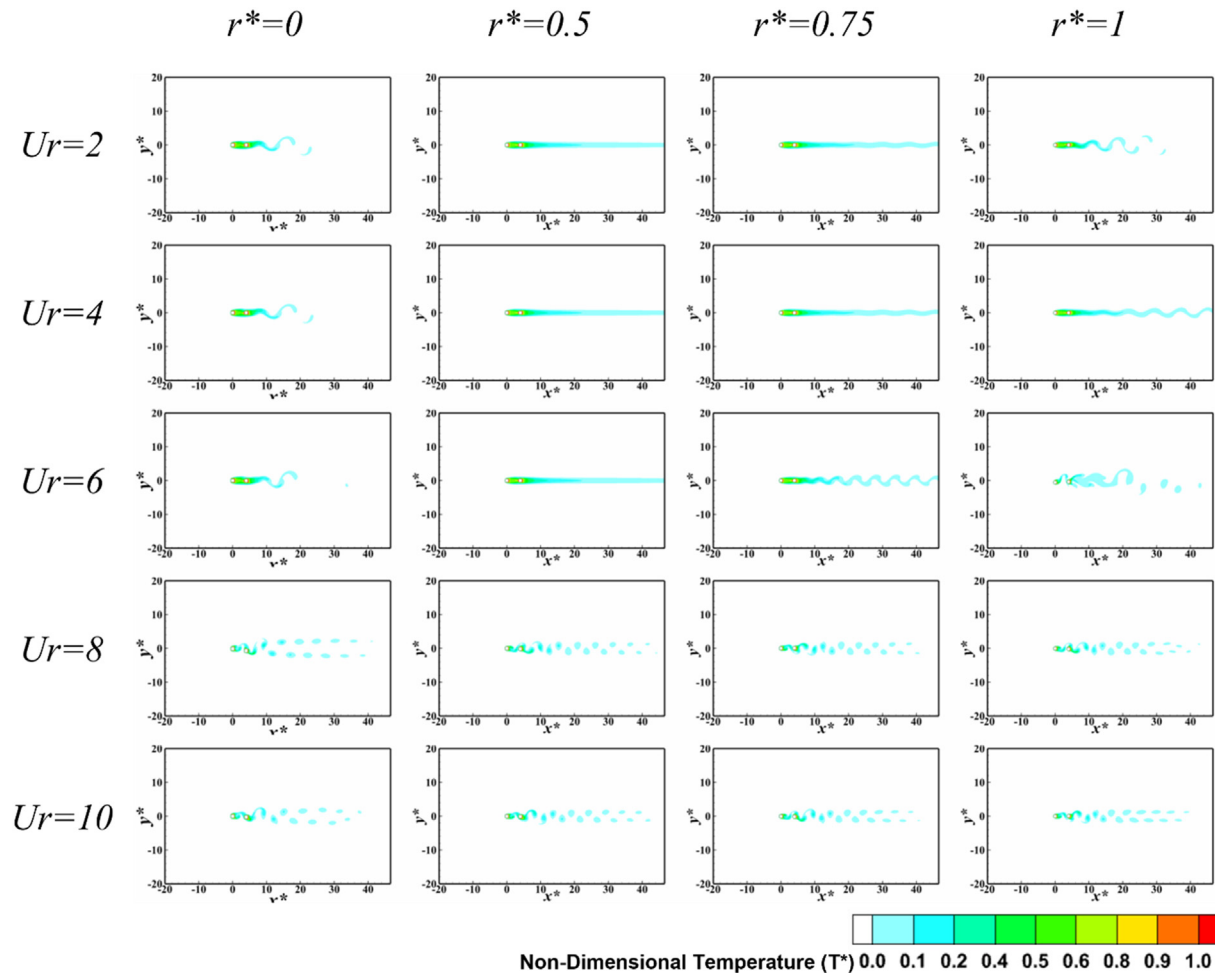


FIG. 11. Non-dimensional temperature contour for both heated cylinders at a constant wall temperature with varying Ur and r^* .

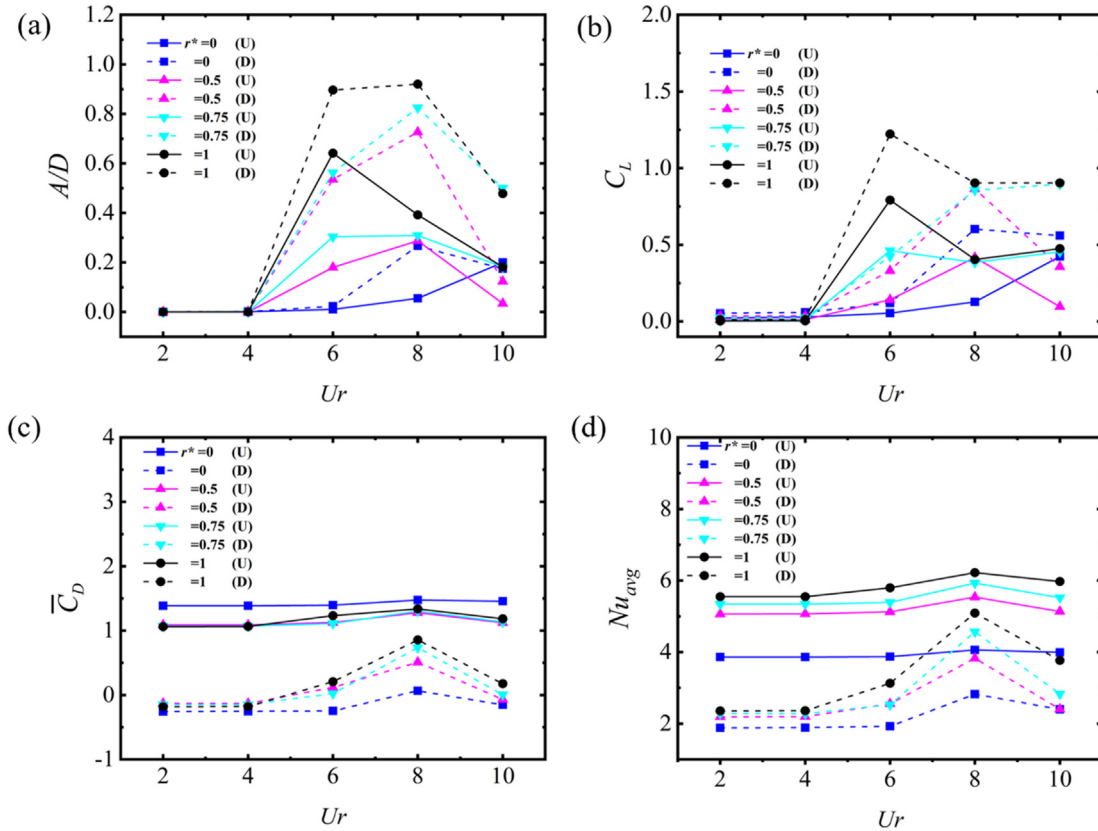


FIG. 12. Effect of r^* on FIV of tandem cylinder by varying Ur . (a) $\frac{A}{D}$ vs Ur , (b) C_L vs Ur , (c) $\overline{C_D}$ vs Ur , and (d) Nu_{avg} vs Ur at $L/D = 2$.

vortices are not able to roll up properly (Lin *et al.*, 2014). A/D of D_C is usually higher than the A/D of U_C . For square cylinder, no vibration is observed for $Ur = 2 \sim 6$. At $Ur = 8$, $r^* = 0.5$ and 0.75 achieve its maximum value, which is same as $r^* = 1$ at $Ur = 6$. A “shift” is observed in values as corner radii are changed from 1 to 0 (Zhao and Zhao, 2019). For square cylinder, maxima is observed at $Ur = 8$, but value is comparatively low as compared to other geometries. At $Ur = 10$, A/D is plummeted to lower values for all cases. This confirms usual behavior of A/D with respect to Ur . A shift is caused for peaks of A/D , which is produced due to change in corner radii. For some cases, a nominal difference in vibrational amplitude can be noticed between U_C and D_C . Vortex shedding from upstream cylinder impinges on the downstream cylinder, which causes fluctuation in all parameters (Borazjani and Sotiropoulos, 2009).

Figure 12(c) illustrates the $\overline{C_D}$ with respect to Ur at varying corner radii. $\overline{C_D}$, in general, is function of forces applied on the body in axial direction. $\overline{C_D}$ of D_C is also dependent on the U_C . Maximum $\overline{C_D}$ is observed for upstream square cylinder at $Ur = 10$, while minimum $\overline{C_D}$ is observed for $Ur = 2$ and 4 . Negative values of $\overline{C_D}$ can be observed for downstream cylinders at lower Ur s, as D_C captured in wake of U_C . Existence of “dead water” between the cylinders shows very low-pressure region, which is very low in comparison with wake of D_C . Net force opposite in axial direction is experienced by the D_C . After $Ur = 6$, D_C is subjected to vibration consequently $\overline{C_D}$ started rising.

Figure 12(b) shows the changes in C_L with respect to reduced velocity for different cases. Vibrational amplitude and C_L are concurrent, and the effect of it is validated from above graphs. At $Ur = 6$, peak in C_L is observed for all cases. Maximum of C_L is observed at $Ur = 6$ for D_C , while lowest is observed for $Ur = 2$ for $r^* = 1$.

Figure 13 shows the time history of A/D for $r^* = 0-1$ in lock-in phase for downstream and upstream cylinder. In most of all the cases, amplitude of downstream cylinder is higher as compared to upstream cylinder. Fluctuations in shear layer of upstream cylinder also affect the vibrational modes of downstream cylinder. A/D for $r^* = 1$ is peaked at $Ur = 6$ as reduced velocity is increased to $Ur = 8$, and amplitude drops to lower values, but C_L persists its nature.

Figure 14 depicts different Z-vorticity contours for all the defined cases at different Ur . Detachment of shear layer followed by rolling of those shear layer due to wake behind the cylinder causes vortex shedding. For $r^* = 0$, U_C overshoots the vortices over D_C and hence acts as “single body,” which is similar to isolated cylinder. 2S type of vortex shedding is observed in these particular cases. Although this regime is dependent on the vibrational modes of both cylinders, $r^* = 0.5, 0.75$, and 1 also show single body regime at lower values of vortex shedding. For $r^* = 0.5$ at $Ur = 6$, as amplitude of D_C overshoots due to the lock-in, which changes the vortices structure in the wake. Shear layer separated from upstream layer is pushed in opposite directions (Sun *et al.*, 2021). In the case of circular cylinder, D_C pushes the vortices to

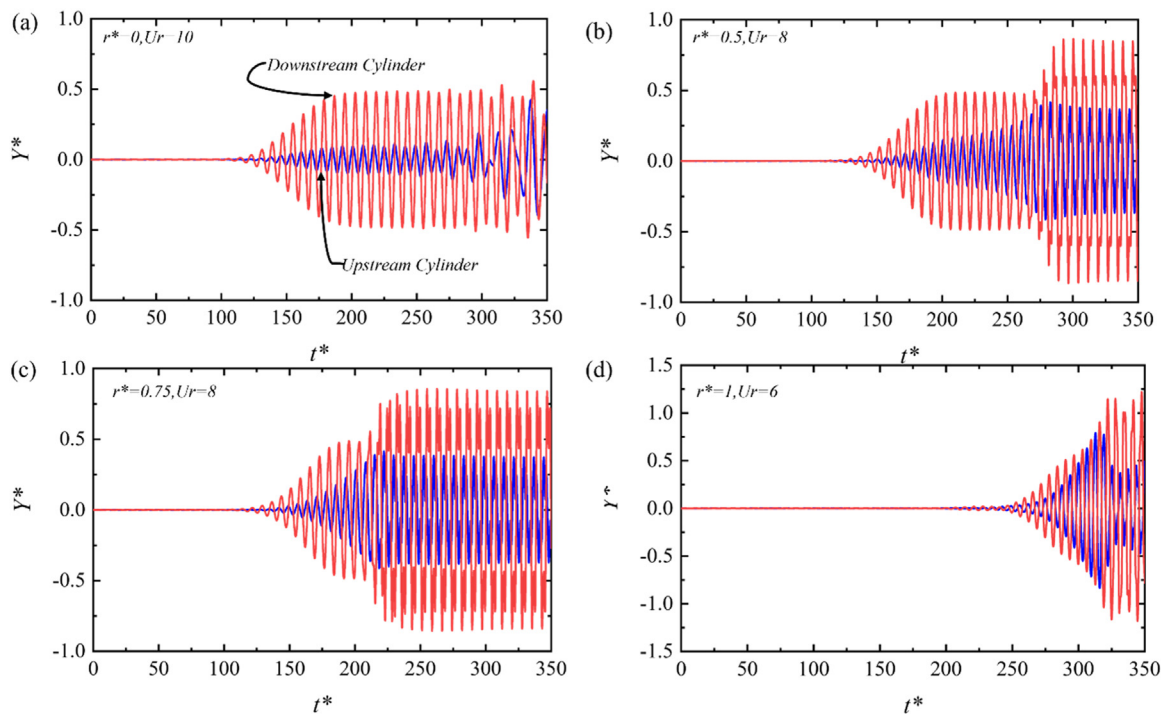


FIG. 13. A/D vs time histories for transversely oscillating tandem cylinder in lock-in phase: (a) $r^* = 0$, $Ur = 10$; (b) $r^* = 0.5$, $Ur = 8$; (c) $r^* = 0.75$, $Ur = 8$; and (d) $r^* = 1$, $Ur = 6$.

the extreme and causes a parallel vortex street. This vortex street is also known as C(2S) vortex shedding (Williamson and Roshko, 1988); hence, D_C also dictates the nature of vortex shedding. As A/D of D_C plummeted with increase in Ur s, vortex shedding is similar to isolated cylinder. A phenomenon of vortex stretching can be observed for $r^* = 0.5$ and 1.

Figure 15 shows the velocity streamlines for some selected cases with varying Ur . For square cylinder at low, Ur shows symmetric wake between the cylinders, while at $Ur = 10$ does not illustrate a stable wake due to the vibration of D_C . A side bubble can be noticed for square cylinder, which caused due to edge separation. $r^* = 0.5$ shows the symmetric wake (recirculation) between cylinder although due to the Coanda effect, flow follows the topology. Topology of figure delays the separation, and side bubble is not visible in this configuration. Oscillating circulation is observed at the rear of D_C . For $r^* = 0.75$ and $Ur = 4$, it shows asymmetric circulation between upstream and downstream cylinder. Higher vibration amplitude destabilizes the wake and eliminates the low-pressure region between the cylinders. Circular cylinder has highest of vibrations for downstream cylinder, and a prominent difference can be observed at $Ur = 6$ and $Ur = 8$. Figure 15 illustrates that vortex for $Ur = 6$ is pushed in a parallel manner, while vortices for $Ur = 8$ are in inline manner.

Figure 16 instantaneous pressure and velocity contour plots for $r^* = 0-1$ at $L/D = 2$. Spacing ratio is reduced to 2; hence, mostly single body effect can be noticed in most of the cases. “Dead water” can be observed between the cylinders when D_C is not having dynamic response. Due to 2S type of vortex shedding, the pressure behind the downstream cylinder is fluctuating. $r^* = 1$ and $Ur = 6$ have larger

wakes due to C(2S) type of vortex shedding. Downstream cylinder pushes the shear layers from upstream cylinder to create two parallel streets; hence, low-pressure region is created between the parallel streets.

Vortex shedding characteristics of vortex shedding are captured by contours of f_s/f_n and power spectral density in Figs. 17 and 18. Figures 17(a) and 17(b) show the ratio of natural frequency and vortex shedding frequency. Lock-in period exists around $f_s/f_n = 1$. From the Figs. 17(a) and 17(b), it is evident that lock-in for U_C and D_C occurs around $Ur = 6$ and 8 (Mysa et al., 2016). Synchronization remained persisted at the same values of Ur for $r^* = 1, 0.50$, and 0.75 . As corner radius starts to decrease, the shift does not occur in case for $L/D = 2$ as compared to $D/D = 4$. Both upstream and downstream cylinders try to resist this shift, but fluctuation in U_C will cause change in D_C .

Figures 18(a)–18(d) illustrate the primary shedding frequency for $r^* = 0-1$ at $Ur = 6 (L/D = 2)$. Shedding frequency of $r^* = 0$ is lower than the natural frequency ($f_n = 0.166$) although values have increased as compared to $L/D = 4$. $r^* = 0.5$ results differ from as $r^* = 0$, $f^*(r^* = 0.5)$ escalated quickly and approaching the f_n showing a huge leap in vibration amplitude as well. Values of downstream cylinder and upstream cylinder frequency are similar in terms of absolute values.

Shedding frequency at $r^* = 1$ and 0.75 shows similar values at $Ur = 6$. f^* for $r^* = 1, 0.75$, and 0.5 impending the natural frequency ($f_n = 0.166$). A second peak is observed for $r^* = 1$ and $r^* = 0.5$ illustrating frequency modulation (f_{mod}) around 0.4. Figures 18(e)–18(h) depict the shedding frequency at $Ur = 8$ for $r^* = 0-1$. $f^* = 0.125 (U_C/D_C)$ of $r^* = 0$ (square cylinder) exactly overlaps the natural frequency

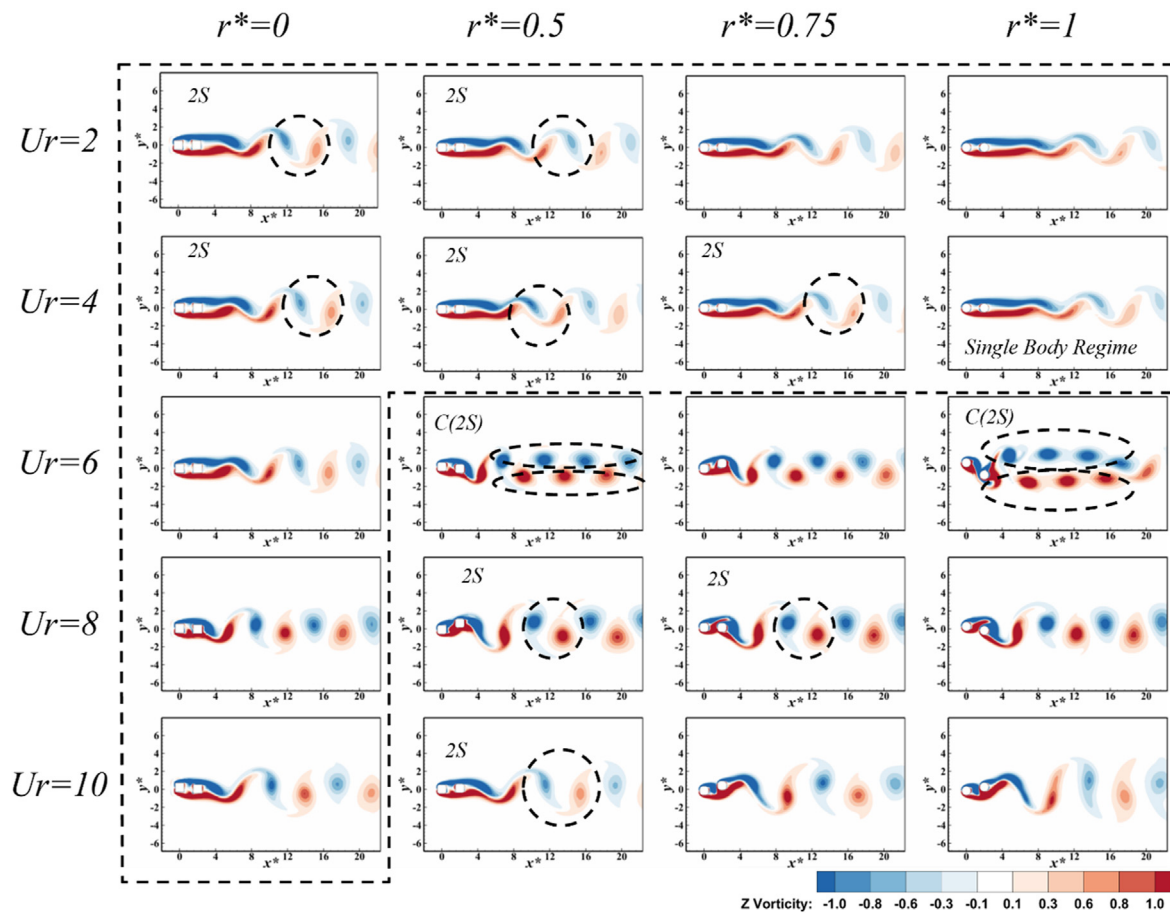


FIG. 14. Z-vorticity contours for varying $r^* = 0-1$ and $Ur = 2 - 10$ for $L/D = 2$.

($f_n = 0.125$) resulting huge vibrational amplitude. No secondary vortex shedding is observed for $r^* = 0$ at $Ur = 8$ (Willden and Graham, 2006; Williamson, 1996). Vortex shedding frequency of $r^* = 0.5, 0.75$, and 1 (D_C/U_C) has dropped as compared to the $r^* = 0$, which is contrary to $L/D = 4$. Frequency modulation can be noticed for $r^* = 0.75$ and 1 as two extra peaks have been observed. Lock-in for $r^* = 0$ occurs as $Ur = 8$, while for $r^* = 0.75$ and 1 , it occurs as $Ur = 6$. At $r^* = 0.5$, it shows larger range for lock-in from $Ur = 6$ to $Ur = 8$.

Figure 19(a) shows phase diagrams for different corner radii at three Ur for U_C and D_C . At $Ur = 4$, for all cases C_L and Y^* appear to be in same phase. At $Ur = 6$, lock-in occurs, which is also shown in the graphs of U_C and D_C at $r^* = 0.75$ and 1 . Amplitude for upstream and downstream cylinder has dropped to a certain lower value contrary to the nature, which is stringent to higher values (Papaioannou et al., 2008). Complete frequency synchronization occurs at $Ur = 8$ in which the vortex shedding frequency collapses exactly upon the natural frequency of the vacuum; hence, the cylinder moves along a periodic orbit in Fig. 19(a). This occurred for U_C and D_C at $Ur = 8$, and “eight” type figures can be observed for $r^* = 0.5, 0.75$, and 1 . For $r^* = 0.5$, U_C phase change occurs at $Ur = 6$ contrary to other configurations of U_C and D_C , which have opposite direction of amplitude and

lift due to phase change. Figure 19(b) shows the instantaneous position of cylinder. It depicts the positions of U_C and D_C , which are opposite sign when one cylinder is at maxima.

The Nusselt number is dependent on the spacing ratio, corner radii, and flow topology around the cylinders (Zhou and Yiu, 2006). Figures 20(a)–20(d) demonstrate the dependence of Nu on θ for $Ur = 6$ at $r^* = 0-1$ ($L/D = 2$). Spacing ratio does not affect the Nu for the frontal area of cylinder as square cylinder has higher Nu , which is same as $L/D = 4$. At $\theta = 45^\circ$, it depicts the rise for Nu due to sharp edge. Heat transfer after 45° started plummeting due to side bubble for $r^* = 0$. Rear separation can also be observed for square cylinder around $\theta = 135^\circ$. For $r^* = 0.5$, D_C has registered a growth in Nu as compared to the $L/D = 4$ due to shift in vibrational amplitude. $Nu(D_C)$ for $r^* = 0.5$ started dropping after $\theta = 65^\circ$ due to shear layer separation. As shown in Fig. 20, separation from downstream cylinder is almost at the same angle as upstream as separation is dependent on the geometry. For spacing ratio of 2, angle of reattachment and angle of separation are entirely different due to overshooting of vortices from U_C . Hence, spacing ratio dictates the separation point from downstream cylinder. For $r^* = 0.5$, separation at $L/D = 4$ occurs around $\theta = 45^\circ - 50^\circ$, while for $L/D = 2$, it has shifted to

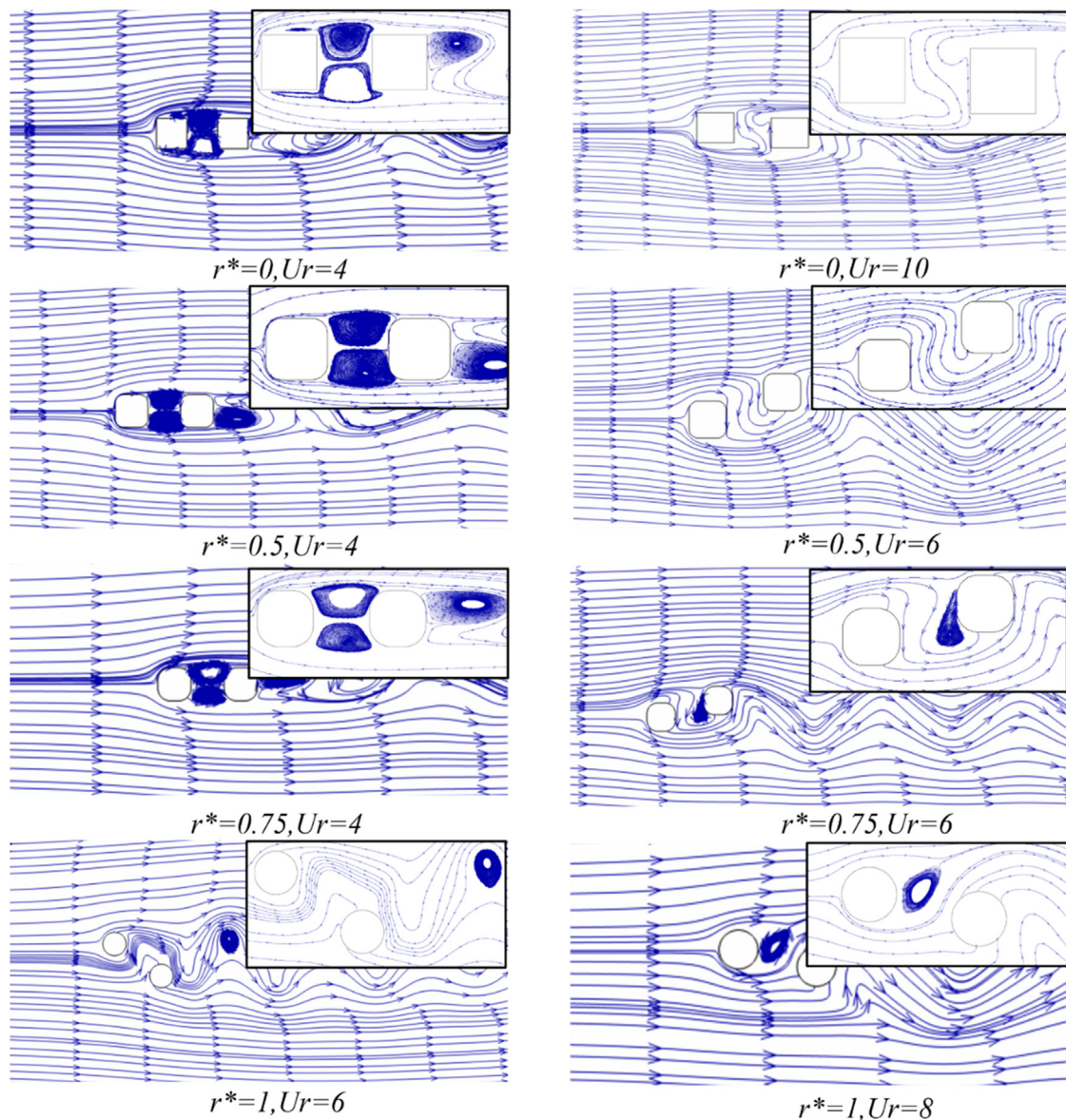


FIG. 15. Velocity streamlines for different cases show casing variants of wake behind the cylinders for spacing ratio of 2.

$\theta = 65^\circ - 70^\circ$. Identical characteristics are shown by $r^* = 0.5$ and $r^* = 0.75$. For circular cylinder, a perfect curve is followed as 0° , which has highest Nu . Along the circular cylinder, sudden drop can be observed in Nu for circular cylinder indicating flow separation due to adverse pressure gradient.

Figures 20(e)–20(h) depict the polar graph between Nu and θ for $Ur = 8$ at $r^* = 0-1$. The purpose of illustrating polar graphs at two different reduced velocities with spacing ratio is to comprehend the effect of vibrational amplitude at transitional level. For $r^* = 0$, $Nu(D_C)$ has three points of separation for downstream cylinder starting from leading-edge separation to trailing edge separation. Point of separation has delayed for $r^* = 0.5$ (D_C) and $r^* = 0.75$ (D_C) as compared to

upstream cylinder for same configurations. Due to less interaction at frontal surface of D_C ($r^* = 0.5$), it causes drop in heat transfer. At filleted area ($\theta = 45^\circ$), a rise of Nu is observed generating “butterfly” shape in Fig. 20(f). Figure 20 shows the temperature variation around the cylinder when it is maintained on a constant temperature. Nu_{avg} of downstream cylinder is highly dependent on the Nu_{avg} of upstream cylinder. Heated flow from upstream cylinder interacts with downstream cylinder. Overall, Nu_{avg} is dependent on flow topology and vibrational amplitude (Zhou and Mahbub Alam, 2016). Higher vibrational amplitude led to the higher Nu_{avg} . Figure 11(d) shows variation in the Nusselt number with respect to Ur with corner radii. Upstream cylinder of square cylinder has least U_C in comparison with other

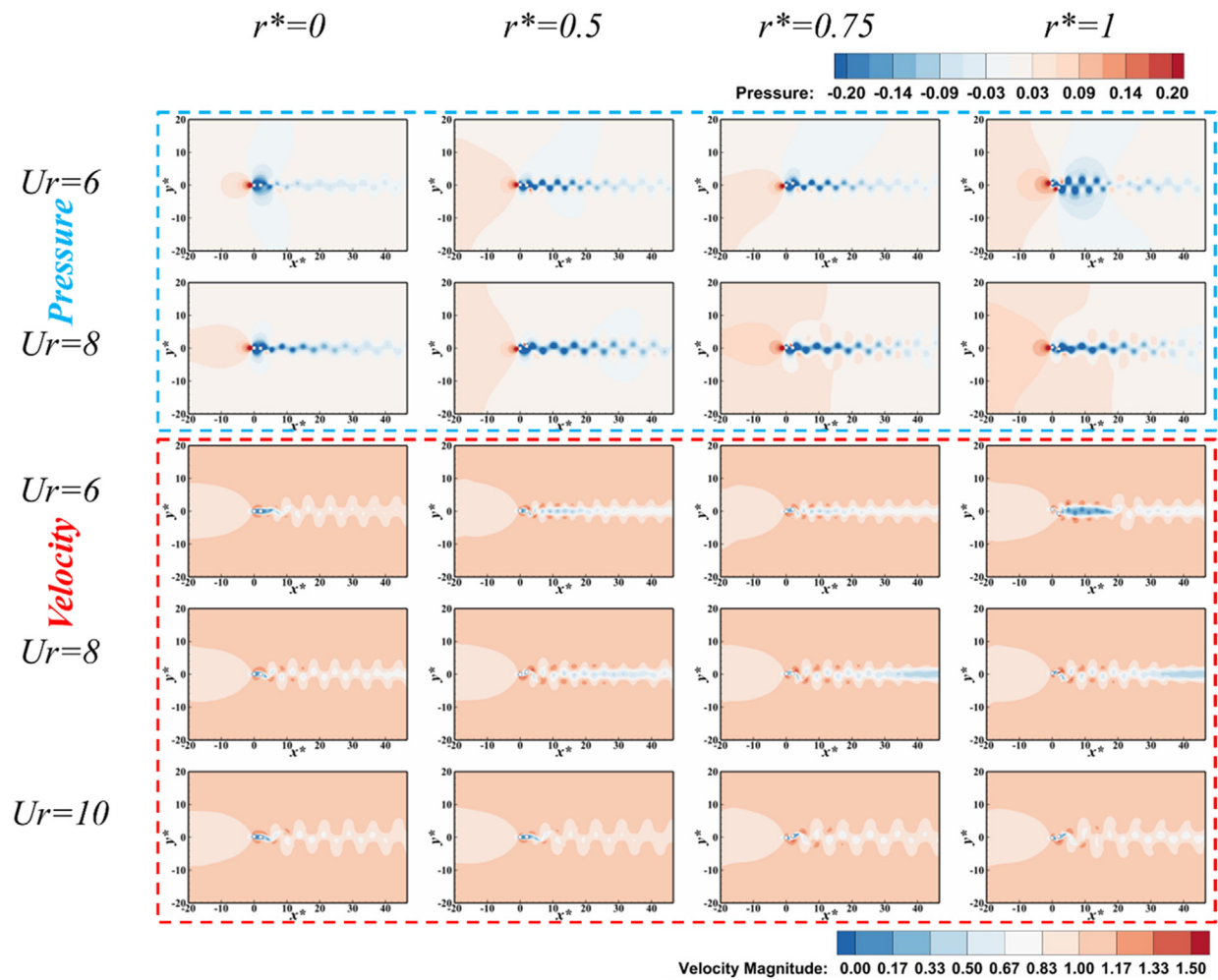


FIG. 16. Instantaneous contour plots of pressure marked in cyan for $r^* = 0-1$ at $Ur = 6$ and 8 with velocity contours marked in red for $r^* = 0-1$ at $Ur = 6, 8$, and 10 with spacing $L/D = 4$.

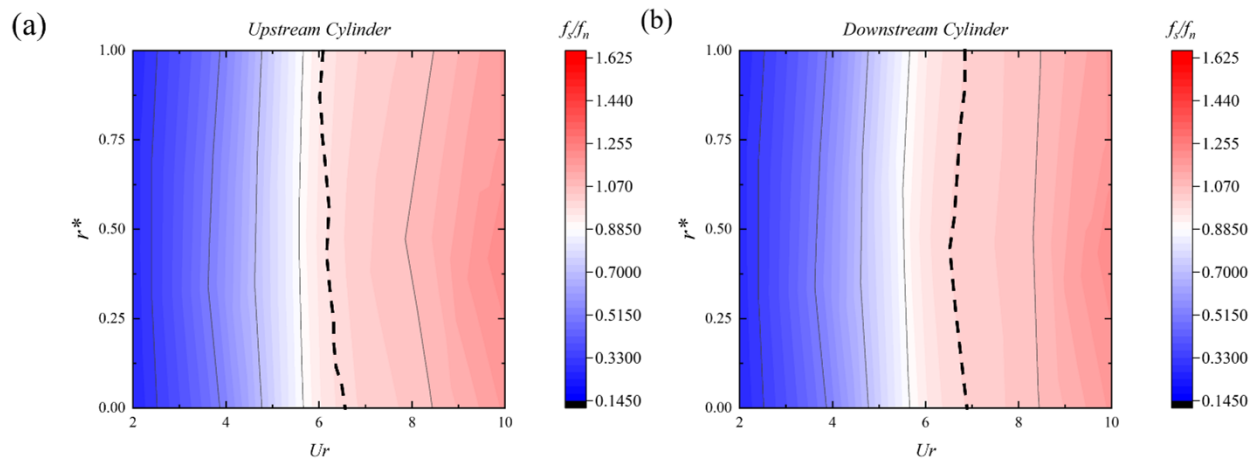


FIG. 17. Contours of f_s/f_n frequency response at $L/D = 2$ of (a) upstream cylinder and (b) downstream cylinder with varying r^* and Ur .

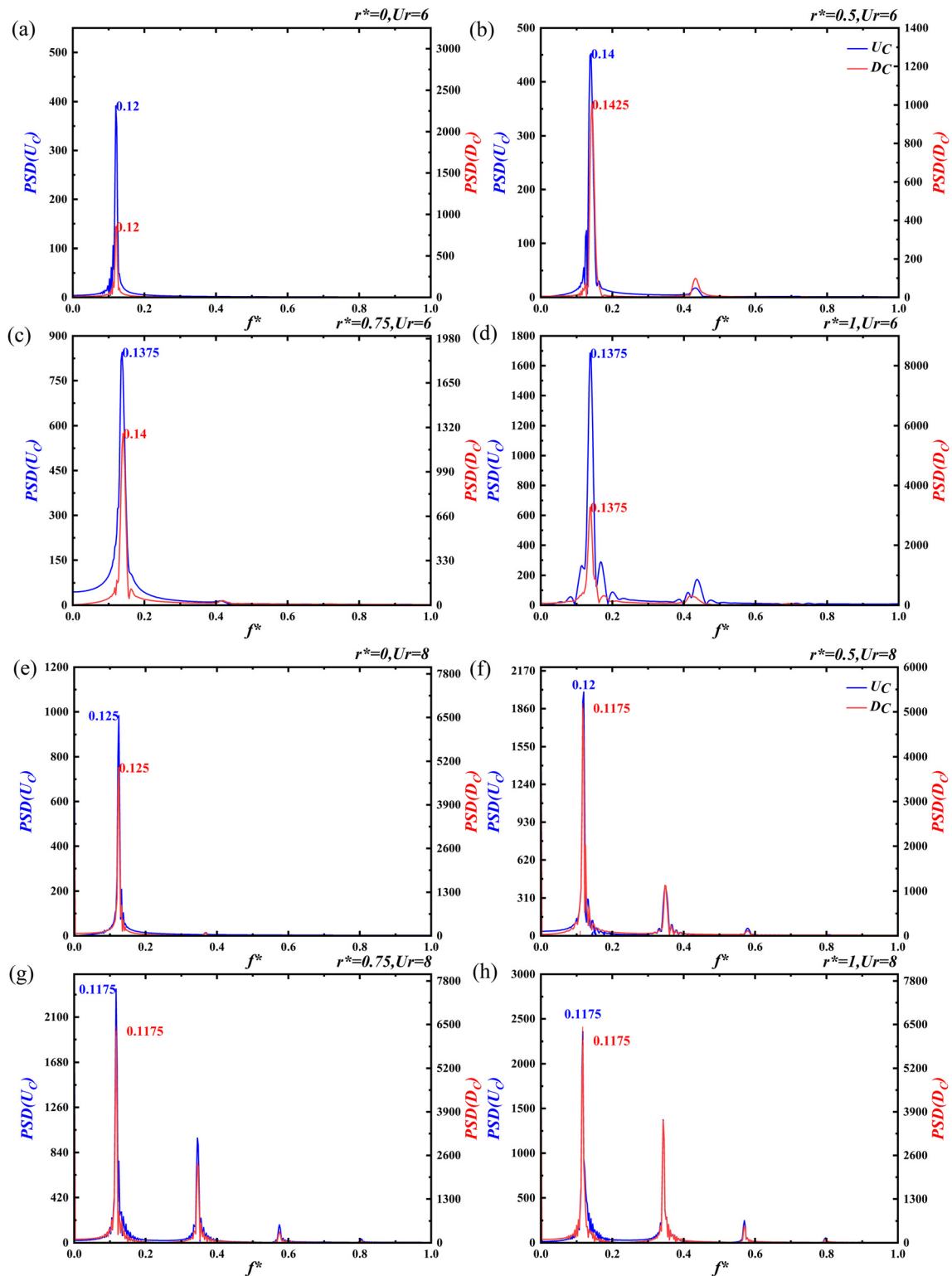


FIG. 18. Power spectral density of lift coefficient for $L/D = 2$ at reduced velocity $Ur = 6$ and 8 , (a)–(e) $r^* = 0$ (square cylinder), (b)–(f) $r^* = 0.5$, (c)–(g) $r^* = 0.75$, and (d)–(h) $r^* = 1$ (circular cylinder).

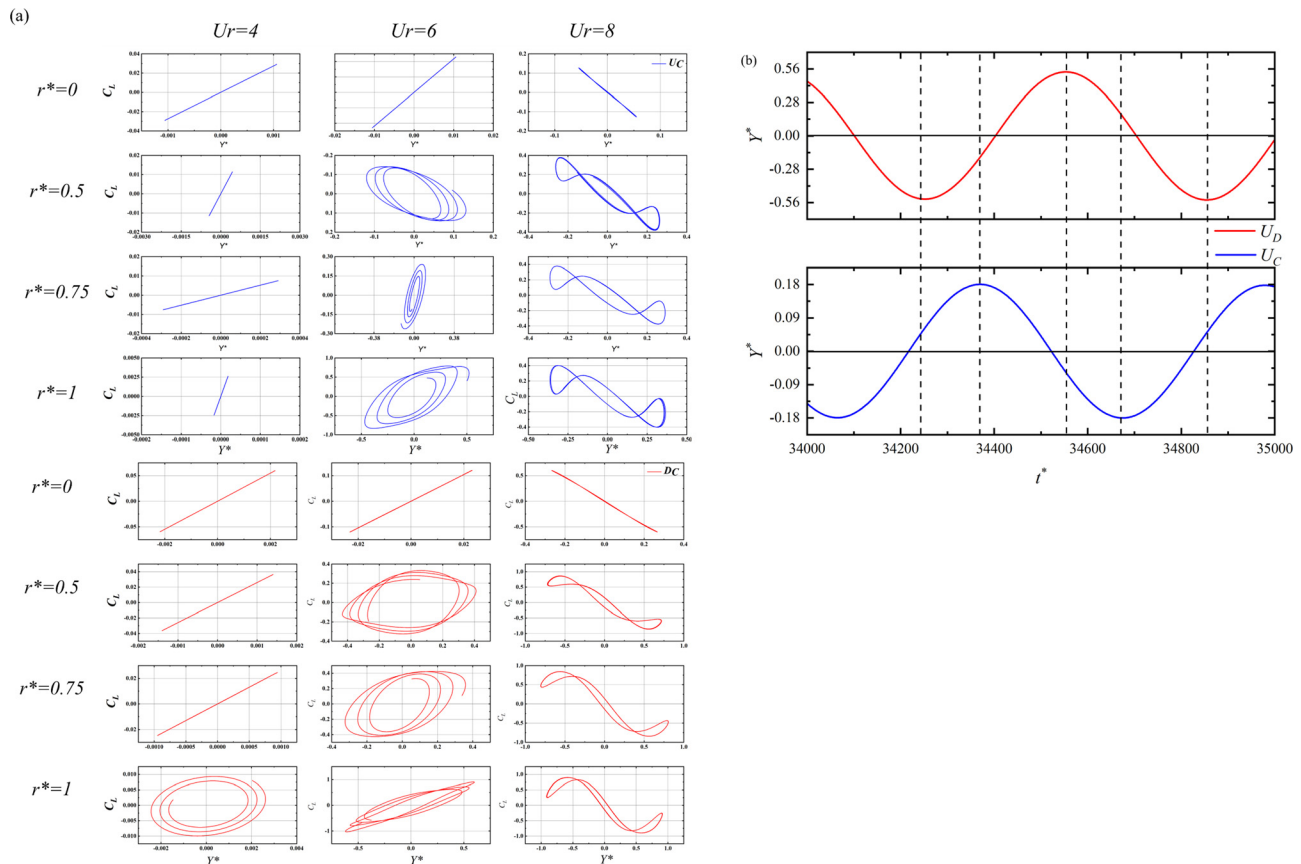


FIG. 19. (a) Phase diagram of upstream cylinder (Blue Grid) and downstream cylinder (Red Grid) at $Ur = 2, 4$, and 8 for $L/D = 2$ and (b) time history for amplitude of $r^* = 0.5$ and $Ur = 6$.

configurations. Flow separation for $r^* = 0$ occurs at the leading edge of square cylinder, which is main cause of less Nu_{avg} . Figure 21 demonstrates the non-dimensional temperature changes around the upstream cylinder when it is maintained at a constant temperature. Upcoming flow sets to be at $T^* = 0$, $Re = 150$, and $Pr = 0.7$, while both cylinders' surface are held at $T^* = 1$. White color ($T^* = 0$) in domain signifies the presence of unaffected area from heat transfer around the cylinder, while affected area is shown by colored contour given in Fig. 21. Temperature contours are similar to vortex shedding patterns as vortices carry heat after shear layer separation.

Nu_{avg} of D_C is less than Nu_{avg} of U_C due to plummeted flow interaction at the rear of upstream cylinder. Circular cylinder shows maximum values of Nu_{avg} due to delayed flow separation causing higher heat transfer to shear layers (Zhang et al., 2019). At $Ur = 6$, $r^* = 1$ shows higher values as compared to $Ur = 4$ for D_C ; A/D of D_C gained momentum and start interacting to upcoming flow rather than flow passing from U_C . Nu_{avg} of $r^* = 1$ experience maxima at $Ur = 8$, while a sharp drop is observed at $Ur = 10$. At $L/D = 2$, Nu_{avg} have a lower value of D_C as compared to D_C of $L/D = 4$. Better heat transfer occurs in "reattachment" as compared to "single body." This is defining the flow topology over the downstream cylinder and deifies the completed dependence of Nu_{avg} at A/D .

IV. CONCLUSION

The effect of spacing ratio and corner radius on forced convection from tandem cylinders is numerically investigated. For all cases, major parameters such as Reynolds number = 150, Prandtl number = 0.7, mass ratio = 10, and damping ratio = 0 are fixed. Reduced velocity varied $Ur = 2-10$ while two different spacing ratio $L/D = 2$ and 4 . Four corner radii (r^*) of cylinder varying from 0, 0.5, and 0.75 to 1 are employed. Major observations are summarized as follows:

- Effect of corner radius illustrates the varying flow topology over the cylinders. Square cylinders show the leading-edge separation with side bubble, while circular cylinder depicts the separation past front surface with primary wake. Delayed flow separation can be observed in $r^* = 1$ and 0.75. Symmetric and asymmetric wakes have been observed with change in Ur , r^* , and $\frac{L}{D}$.
- For $L/D = 4$, maxima of vibrational amplitude are observed for D_C at $r^* = 1$ while minima occurred at $Ur = 2$ for $r^* = 0$. Maximum $\overline{C_D}$ is noted for $r^* = 1$ for upstream cylinder, which occurred due to large wake behind the cylinder. Negative value of $\overline{C_D}$ is discovered, which explains the presence of "dead water" between the cylinders. Lock-in for $r^* = 0$ and 0.5 occurs at around $Ur = 8$, while for $r^* = 0.75$ and 1, it occurs at $Ur = 6$.

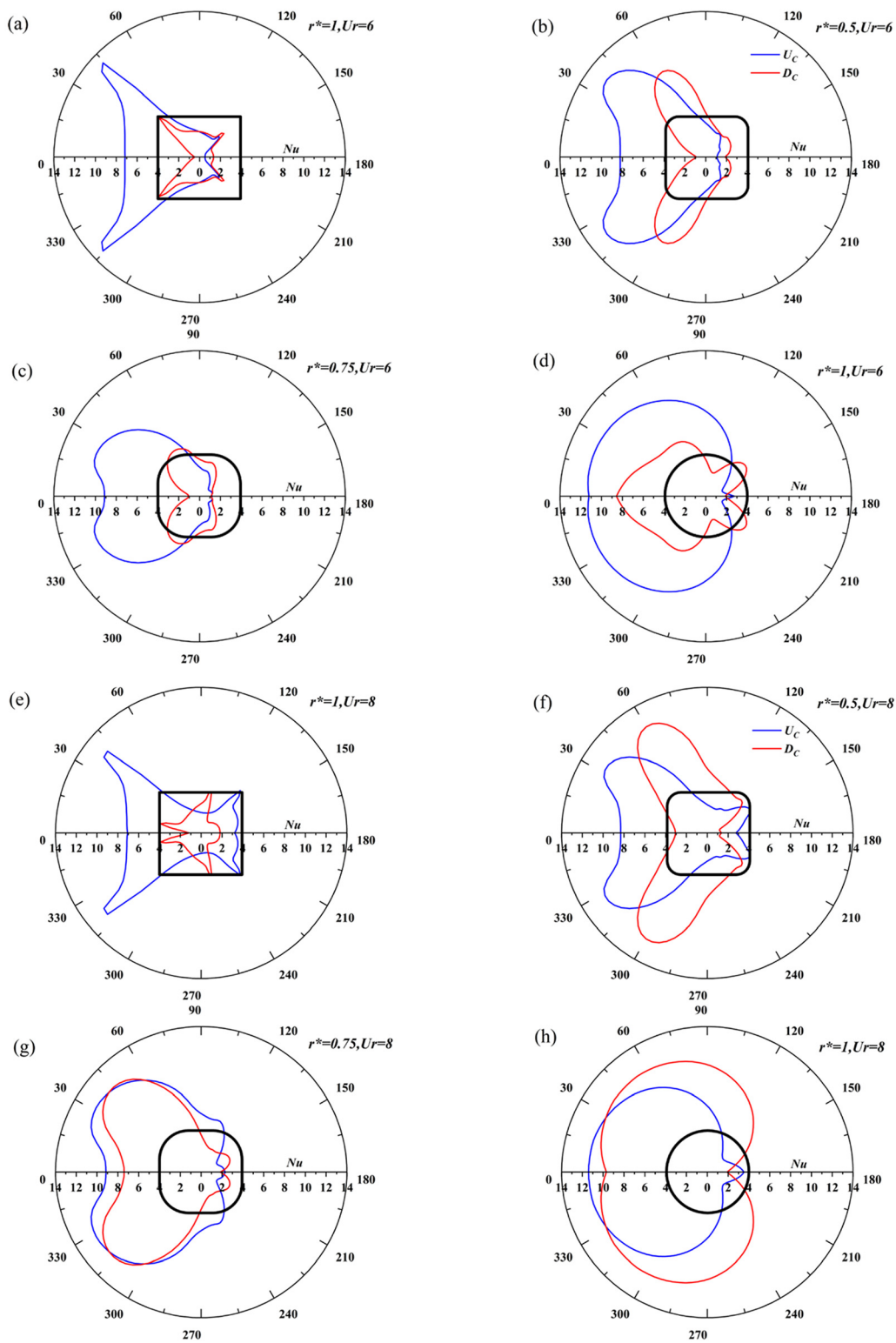


FIG. 20. Dependence on θ point-averaged Nusselt number Nu for $L/D = 2$ at reduced velocity $Ur = 6$ and 8 , (a)–(e) $r^* = 0$ (square cylinder), (b)–(f) $r^* = 0.5$, (c)–(g) $r^* = 0.75$, and (d)–(h) $r^* = 1$ (circular cylinder).

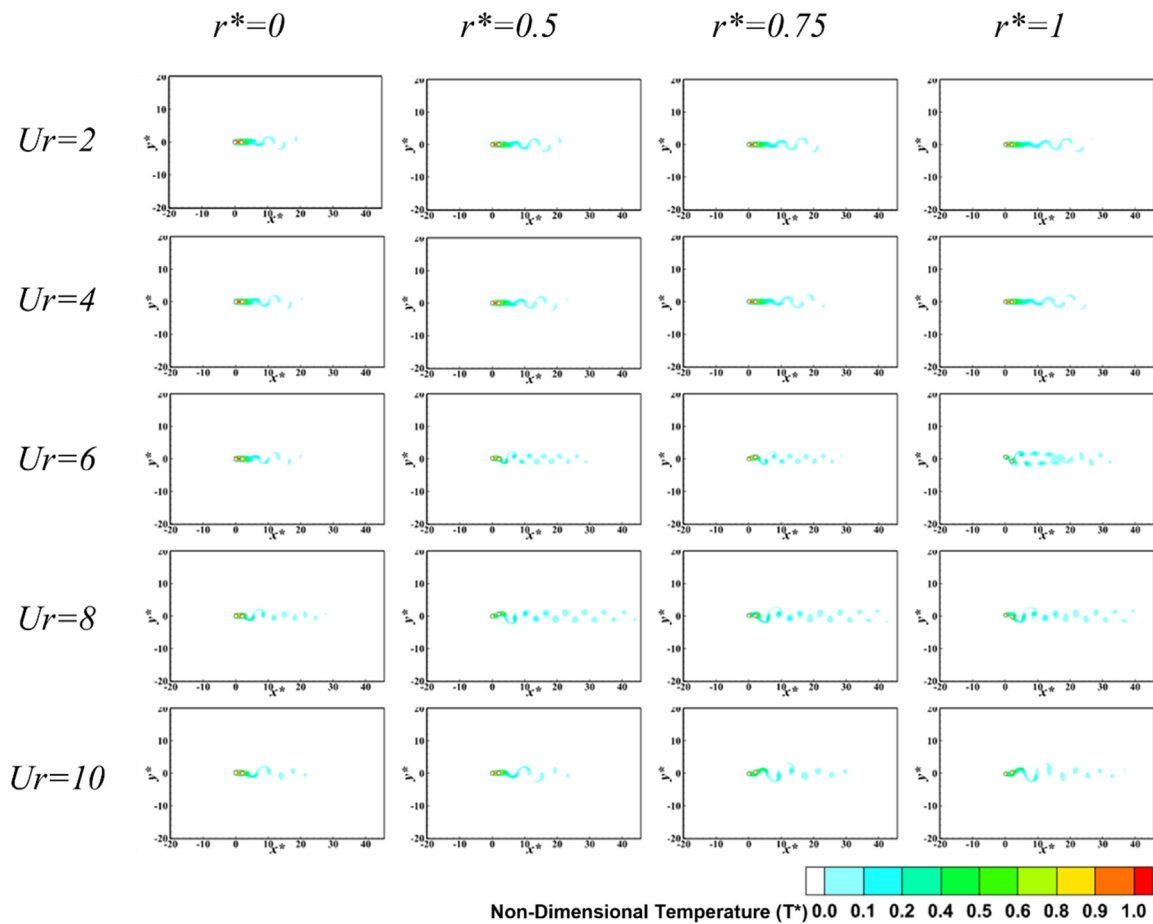


FIG. 21. Temperature contour for both heated cylinder at a constant wall temperature with varying Ur and r^* .

This phenomenon is termed as “shift.” Direction of forces on cylinder changes due to change in Ur . At $Ur = 4$, for all cases C_L and Y^* appear to be in same phase. At $Ur = 6$, lock-in occurs, which is also shown in the phase diagrams of U_C and D_C . At $r^* = 0.75$ and 1 ($Ur = 6$) are in same phase while phase lag observed at $Ur = 8$. For all cases, phase change is occurred when Ur changes from 6 to 8.

- Different type of vortex shedding has been observed along with various flow patterns. Flow patterns are closely related to shear layer separation. Changes in shear layer separation can cause complicated wake interaction and chaotic shedding. Except square cases, most of the cases have shown reattachment after separation. Vortex shedding from tandem cylinder is either C(2S) or 2S.
- For $Ur = 6$, f^* for $r^* = 1$ and 0.75 approaching the natural frequency ($f_n = 0.166$). A second peak is observed for $r^* = 1$ and $r^* = 0.75$ illustrating frequency modulation. At $Ur = 8$, vortex shedding frequency of $r^* = 0.75$ and $r^* = 1$ (D_C/U_C) is impending the natural frequency ($f_n = 0.125$) causing synchronization. Frequency modulation can be observed from the power spectral density.
- For square cylinder, the frontal area has higher Nu because frontal area is in direct contact of upcoming flow. At $r^* = 0.75$, a

smooth curved is followed as started from lower to higher Nu at corner of geometry. For circular cylinder, a perfect curve is followed as 0° have highest Nu . Along the circular cylinder, sudden drop can be observed in Nu for circular cylinder indicating flow separation due to adverse pressure gradient. Vibration amplitude affects the local Nu due to change in vibrational modes. Forced convection on the tandem cylinders in this study is dependent on major factors such as A/D , flow topology, spacing ratio, and corner radii. Higher vibration in tandem cylinders adds in the value Nu_{avg} . Maximum value of Nu_{avg} is at $r^* = 1$ and $Ur = 6$ for $L/D = 4$ (U_C), while minimum is recorded at $r^* = 0$ and $Ur = 2$ (D_C).

- At $L/D = 2$, flow characteristics becomes simpler. Maximum A/D is observed for $r^* = 1$ (D_C) at $Ur = 6$. For $r^* = 1$ and $Ur = 6$, lock-in occurs along with C(2S) type of vortex shedding. Phases illustrate the force's direction and force response on vibrational amplitude. At $Ur = 4$, C_L and Y^* appear to be in same phase. Complete frequency synchronization occurs at $Ur = 8$ in which the vortex shedding frequency collapses exactly upon the natural frequency of the cylinder; hence, the cylinder moves along a periodic orbit.
- Lock-in period exist around $f_s/f_n = 1$. Contour graphs supported that phenomenon (lock-in) for U_C and D_C occurs around

$Ur = 6$ and 8 . Synchronization remained persisted at the same values of Ur for $r^* = 1, 0.50$, and 0.75 . The “shift” did not occur in case for $L/D = 2$ as compared to $D = 4$. Both upstream and downstream cylinders try to resist this shift, but fluctuation in U_C will cause changes in D_C .

- Steady flow along with “single body” regime can be observed at lower Urs . For $Ur = 6$ at $r^* = 0.5$ and 1 , it depicts C(2S) type of vortex shedding, which occurred due to interaction of vortices from lower surface and upper surface of D_C . A parallel vortex street is created by pushing the shear layer, which is approaching from upstream cylinder.
- For $L/D = 4$, separation from downstream cylinder is almost at the same angle as upstream as separation is dependent on the geometry. For spacing ratio of 2 , angle of reattachment and angle of separation are entirely different due to overshooting of vortices from U_C . Hence, spacing ratio dictates the separation point from downstream cylinder. For $r^* = 0.5$, separation at $L/D = 4$ occurs around $\theta = 45^\circ - 50^\circ$, while for $L/D = 2$, it has shifted to $\theta = 65^\circ - 70^\circ$. Along the circular cylinder, sudden drop can be observed in Nu for circular cylinder indicating flow separation due to adverse pressure gradient. The purpose of illustrating polar graphs at two different reduced velocities with spacing ratio is to comprehend the effect of vibrational amplitude at transitional level. For $r^* = 0$, $Nu(D_C)$ have three points of separation for downstream cylinder starting from leading-edge separation to trailing-edge separation. For $L/D = 2$, maximum Nu_{avg} occurs at $r^* = 1$ and $Ur = 6$ (U_C), while minimum lies on $r^* = 0$ and $Ur = 2$ (D_C). At $L/D = 2$, Nu_{avg} have a lower value of D_C as compared to D_C of $L/D = 4$. Better heat transfer occurs in “reattachment” as compared to “single body.”

ACKNOWLEDGMENTS

This study was supported by Khalifa University of Science and Technology, Abu Dhabi, UAE, through Grant CIRA-2020-057. We gratefully acknowledge this support.

AUTHOR DECLARATIONS

Conflict of Interest

The authors have no conflicts to disclose.

Author Contributions

Yuvraj Sarout: Data curation (equal); Formal analysis (equal); Methodology (equal); Software (equal); Validation (equal); Writing – original draft (equal). **Md Islam:** Conceptualization (equal); Funding acquisition (equal); Investigation (equal); Methodology (equal); Project administration (equal); Supervision (equal); Writing – review & editing (equal). **Yit Fatt Yap:** Conceptualization (equal); Methodology (equal); Supervision (equal); Writing – review & editing (equal). **Isam Janajreh:** Conceptualization (equal); Methodology (equal); Supervision (equal).

DATA AVAILABILITY

The data that support the findings of this study are available within the article.

REFERENCES

- Adeeb, E., Haider, B. A., and Sohn, C. H., “Influence of rounded corners on flow interference between two tandem cylinders using FVM and IB-LBM,” *HFF* **28**, 1648–1663 (2018).
- Ajith Kumar, R., Sohn, C. H., and Gowda, B. H. L., “Influence of corner radius on the near wake structure of a transversely oscillating square cylinder,” *J. Mech. Sci. Technol.* **23**, 2390–2416 (2009).
- Alam, Md. M., Bai, H., and Zhou, Y., “The wake of two staggered square cylinders,” *J. Fluid Mech.* **801**, 475–507 (2016).
- Alam, M., Abdelhamid, T., and Islam, M., “Heat transfer and flow around cylinder: Effect of corner radius and Reynolds number,” *Int. J. Heat Mass Transfer* **171**, 121105 (2021).
- Alam, M., Abdelhamid, T., and Sohankar, A., “Effect of cylinder corner radius and attack angle on heat transfer and flow topology,” *Int. J. Mech. Sci.* **175**, 105566 (2020).
- Alam, M., Moriya, M., Takai, K., and Sakamoto, H., “Fluctuating fluid forces acting on two circular cylinders in a tandem arrangement at a subcritical Reynolds number,” *J. Wind Eng. Ind. Aerodyn.* **91**, 139–154 (2003).
- Ali, U., Islam, M., and Janajreh, I., “Heat transfer and wake-induced vibrations of heated tandem cylinders with two degrees of freedom: Effect of spacing ratio,” *Phys. Fluids* **34**, 113612 (2022a).
- Ali, U., Islam, M. D., and Janajreh, I., “Flow over rotationally oscillating heated circular cylinder at low Reynolds number,” *Ocean Eng.* **265**, 112515 (2022b).
- Ali, U., Islam, M., Janajreh, I., Fatt, Y., and Alam, M., “Flow-induced vibrations of single and multiple heated circular cylinders: A review,” *Energies* **14**, 8496 (2021).
- Bao, Y., Huang, C., Zhou, D., Tu, J., and Han, Z., “Two-degree-of-freedom flow-induced vibrations on isolated and tandem cylinders with varying natural frequency ratios,” *J. Fluids Struct.* **35**, 50–75 (2012).
- Borazjani, I., and Sotiropoulos, F., “Vortex-induced vibrations of two cylinders in tandem arrangement in the proximity-wake interference region,” *J. Fluid Mech.* **621**, 321–364 (2009).
- Chaplin, J. R., Bearman, P. W., Huera Huarte, F. J., and Pattenden, R. J., “Laboratory measurements of vortex-induced vibrations of a vertical tension riser in a stepped current,” *J. Fluids Struct.* **21**, 3–24 (2005).
- Chen, W., Ji, C., Williams, J., Xu, D., Yang, L., and Cui, Y., “Vortex-induced vibrations of three tandem cylinders in laminar cross-flow: Vibration response and galloping mechanism,” *J. Fluids and Struct.* **78**, 215–238 (2018).
- Cheng, L., Luan, T., Du, W., and Xu, M., “Heat transfer enhancement by flow-induced vibration in heat exchangers,” *Int. J. Heat Mass Transfer* **52**, 1053–1057 (2009).
- Derakhshandeh, J. F., and Alam, M. M., “A review of bluff body wakes,” *Ocean Eng.* **182**, 475–488 (2019).
- Dhiman, A. K., Chhabra, R. P., Sharma, A., and Eswaran, V., “Effects of Reynolds and Prandtl numbers on heat transfer across a square cylinder in the steady flow regime,” *Numer. Heat Transfer Part Appl.* **49**, 717–731 (2006).
- Dwivedi, A. R., and Dhiman, A. K., “Flow and heat transfer analysis around tandem cylinders: Critical gap ratio and thermal cross-buoyancy,” *J. Braz. Soc. Mech. Sci. Eng.* **41**, 487 (2019).
- Gao, D., Zhang, S., Ning, Z., Chen, W.-L., and Li, H., “On the coupling mechanism of rain-wind two-phase flow induced cable vibration: A wake-dynamics perspective,” *Phys. Fluids* **33**, 117102 (2021).
- Gourari, S., Mebarek-Oudina, F., Hussein, A., Kolsi, L., Hassen, W., and Younis, O., “Numerical study of natural convection between two coaxial inclined cylinders,” *IJHT* **37**, 779–786 (2019).
- Gray, A., Smith, L., Weiland, M. (Eds.), in *Proceedings of the 3rd International Conference on Exascale Applications and Software: EASC 2015, 21–23 April 2015* (Edinburgh UK, University of Edinburgh, Edinburgh, 2015).
- Griffith, M. D., Jacono, D. L., Sheridan, J., and Leontini, J. S., “Flow-induced vibration of two cylinders in tandem and staggered arrangements,” *J. Fluid Mech.* **833**, 98–130 (2017).
- Hu, J., Zhou, Y., and Dalton, C., “Effects of the corner radius on the near wake of a square prism,” *Exp. Fluids* **40**, 106–118 (2006).
- Hu, J. C. and Zhou, Y., “Flow structure behind two staggered circular cylinders. Part 2. Heat momentum transport,” *J. Fluid Mech.* **607**, 81–107 (2008).

- Huera-Huarte, F. J. and Bearman, P. W., "Vortex and wake-induced vibrations of a tandem arrangement of two flexible circular cylinders with near wake interference," *J. Fluids Struct.* **27**, 193–211 (2011).
- Izadpanah, E., Amini, Y., and Ashouri, A., "A comprehensive investigation of vortex induced vibration effects on the heat transfer from a circular cylinder," *Int. J. Therm. Sci.* **125**, 405–418 (2018).
- Jauvtis, N. and Williamson, C. H. K., "Vortex-induced vibration of a cylinder with two degrees of freedom," *J. Fluids Struct.* **17**, 1035–1042 (2003).
- Ji, J., Zhang, J., Li, F., Chen, Q., Ni, X., and Deng, X., "Numerical research on vibration-enhanced heat transfer of improved elastic tube bundle heat exchanger," *Case Stud. Therm. Eng.* **33**, 101936 (2022).
- Khalak, A. and Charles, H. K. W., "Investigation of relative effects of mass and damping in vortex-induced vibration of a circular cylinder," *J. Wind Eng. Ind. Aerodyn.* **69–71**, 341–350 (1997).
- Khan, H. H., Islam, M., Fatt, Y. Y., Janajreh, I., and Alam, M. M., "Flow-induced vibration on two tandem cylinders of different diameters and spacing ratios," *Ocean Eng.* **258**, 111747 (2022).
- Kumar, D. and Sen, S., "Flow-induced vibrations of a pair of in-line square cylinders," *Phys. Fluids* **33**, 043602 (2021).
- Lin, J.-Z., Jiang, R.-J., and Ku, X.-K., "Numerical prediction of an anomalous biased oscillation regime in vortex-induced vibrations of two tandem cylinders," *Phys. Fluids* **26**, 034102 (2014).
- Liu, C., Fu, S., Zhang, M., Ren, H., and Xu, Y., "Hydrodynamics of a flexible cylinder under modulated vortex-induced vibrations," *J. Fluids Struct.* **94**, 102913 (2020).
- Mahir, N. and Altaç, Z., "Numerical investigation of convective heat transfer in unsteady flow past two cylinders in tandem arrangements," *Int. J. Heat Fluid Flow* **29**, 1309–1318 (2008).
- Miran, S. and Sohn, C. H., "Numerical study of the rounded corners effect on flow past a square cylinder," *Int. J. Numer. Methods Heat Fluid Flow* **25**, 686–702 (2015).
- Mittal, S., Kumar, V., and Raghuvanshi, A., "Unsteady incompressible flows past two cylinders in tandem and staggered arrangements," *Int. J. Numer. Meth. Fluids* **25**, 1315–1344 (1997).
- Mittal, S. and Kumar, V., "Flow induced oscillations of two cylinders in tandem and staggered arrangements," *J. Fluids Struct.* **15**, 717–736 (2001).
- Mohany, A., Arthurs, D., Bolduc, M., Hassan, M., and Ziada, S., "Numerical and experimental investigation of flow-acoustic resonance of side-by-side cylinders in a duct," *J. Fluids Struct.* **48**, 316–331 (2014).
- Mussa, A., Asinari, P., and Luo, L.-S., "Lattice Boltzmann simulations of 2D laminar flows past two tandem cylinders," *J. Comput. Phys.* **228**, 983–999 (2009).
- Mysa, R. C., Kaboudian, A., and Jaiman, R. K., "On the origin of wake-induced vibration in two tandem circular cylinders at low Reynolds number," *J. Fluids Struct.* **61**, 76–98 (2016).
- Nepali, R., Ping, H., Han, Z., Zhou, D., Yang, H., Tu, J., Zhao, Y., and Bao, Y., "Two-degree-of-freedom vortex-induced vibrations of two square cylinders in tandem arrangement at low Reynolds numbers," *J. Fluids Struct.* **97**, 102991 (2020).
- Papaioannou, G. V., Yue, D. K. P., Triantafyllou, M. S., and Karniadakis, G. E., "On the effect of spacing on the vortex-induced vibrations of two tandem cylinders," *J. Fluids Struct.* **24**, 833–854 (2008).
- Prasanth, T. and Mittal, S., "Vortex-induced vibration of two circular cylinders at low Reynolds number," *J. Fluids Struct.* **25**, 731–741 (2009).
- Qiu, B., Du, B., Huang, C., Chen, W., Yan, J., and Wang, B., "The numerical simulation of the flow distribution and flow-induced vibration analysis for intermediate heat exchanger in a pool-type fast breeder reactor," *Prog. Nucl. Energy* **131**, 103605 (2021).
- Rao, C., Zhang, Y., and Wan, D., "Numerical simulation of the solitary wave interacting with an elastic structure using MPS-FEM coupled method," *J. Mar. Sci. Appl.* **16**, 395–404 (2017).
- Sarout, Y., Islam, M., Fatt, Y., and Janajreh, I., "Flow around an Oscillating Cylinder at Low Reynolds Number with Forced Convection: Effect of Corner Radius and Reynolds Number," *Energies* **15**, 9145 (2022a).
- Sarout, Y., Islam, M. D., Fatt, Y. Y., and Janajreh, I., "Analysis of corner radius on the free oscillating cylinder with heat transfer and flow pattern at low Reynolds number," in *Presented at the ASME 2022 Heat Transfer Summer Conference Collocated with the ASME 2022 16th International Conference on Energy Sustainability* (American Society of Mechanical Engineers Digital Collection, 2022b).
- Sarpkaya, T., "A critical review of the intrinsic nature of vortex-induced vibrations," *J. Fluids Struct.* **19**, 389–447 (2004).
- Sen, S. and Mittal, S., "Free vibration of a square cylinder at low Reynolds numbers," *J. Fluids Struct.* **27**(BBVIV-6), 875–884 (2011).
- Sumner, D., "Two circular cylinders in cross-flow: A review," *J. Fluids Struct.* **26**, 849–899 (2010).
- Sun, X., Li, S., Lin, G.-G., and Zhang, J.-Z., "Effects of flow-induced vibration on forced convection heat transfer from two tandem circular cylinders in laminar flow," *Int. J. Mech. Sci.* **195**, 106238 (2021).
- Wang, E., Xiao, Q., and Incecik, A., "Three-dimensional numerical simulation of two-degree-of-freedom VIV of a circular cylinder with varying natural frequency ratios at $Re = 500$," *J. Fluids Struct.* **73**, 162–182 (2017).
- Wang, W., Wu, M., Palm, J., and Eskilsson, C., "Estimation of numerical uncertainty in computational fluid dynamics simulations of a passively controlled wave energy converter," *Proc. Inst. Mech. E.* **232**, 71–84 (2018).
- Willden, R. H. J. and Graham, J. M. R., "Three distinct response regimes for the transverse vortex-induced vibrations of circular cylinders at low Reynolds numbers," *J. Fluids Struct.* **22**, 885–895 (2006).
- Williamson, C. H. K., "Vortex dynamics in the cylinder wake," *Annu. Rev. Fluid Mech.* **28**, 477–539 (1996).
- Williamson, C. H. K. and Govardhan, R., "Vortex-induced vibrations," *Annu. Rev. Fluid Mech.* **36**, 413–455 (2004).
- Williamson, C. H. K. and Roshko, A., "Vortex formation in the wake of an oscillating cylinder," *J. Fluids Struct.* **2**, 355–381 (1988).
- Xiao, Q., Sun, K., Liu, H., and Hu, J., "Computational study on near wake interaction between undulation body and a D-section cylinder," *Ocean Eng.* **38**, 673–683 (2011).
- Xu, W., Zhang, Q., Wang, Q., Pang, T., Ma, Y., and Wang, E., "Flow-induced vibration analysis of two unequal-diameter flexible cylinders in staggered configuration from a hydrodynamic force perspective," *Mar. Struct.* **83**, 103173 (2022).
- Yao, W. and Jaiman, R. K., "Stability analysis of the wake-induced vibration of tandem circular and square cylinders," *Nonlinear Dyn.* **95**, 13–28 (2019).
- Zafar, F. and Alam, M., "Mixed convection heat transfer from a circular cylinder submerged in wake," *Int. J. Mech. Sci.* **183**, 105733 (2020).
- Zdravkovich, M. M., "different modes of vortex shedding: An overview," *J. Fluids Struct.* **10**, 427–437 (1996).
- Zdravkovich, M. M., "The effects of interference between circular cylinders in cross flow†††An earlier version as originally presented as an invited paper, entitled 'Forces on pipe clusters', at the International Symposium on Separated Flow around Marine Structures, Norwegian Institute of Technology, Trondheim, Norway, 26–28 June 1985," *J. Fluids Struct.* **1**, 239–261 (1987).
- Zhang, W., Chen, X., Yang, H., Liang, H., and Wei, Y., "Forced convection for flow across two tandem cylinders with rounded corners in a channel," *Int. J. Heat Mass Transfer* **130**, 1053–1069 (2019).
- Zhao, H. and Zhao, M., "Effect of rounded corners on flow-induced vibration of a square cylinder at a low Reynolds number of 200," *Ocean Eng.* **188**, 106263 (2019).
- Zhao, J., Leontini, J. S., Lo Jacono, D., and Sheridan, J., "Fluid–structure interaction of a square cylinder at different angles of attack," *J. Fluid Mech.* **747**, 688–721 (2014).
- Zhou, Y. and Mahbub Alam, M., "Wake of two interacting circular cylinders: A review," *Int. J. Heat Fluid Flow* **62**, 510–537 (2016).
- Zhou, Y. and Yiu, M. W., "Flow structure, momentum and heat transport in a two-tandem-cylinder wake," *J. Fluid Mech.* **548**, 17–48 (2006).
- Zhu, H. B., Ping, H., Wang, R., Bao, Y., Zhou, D., and Han, Z. L., "Flow-induced vibration of a flexible triangular cable at low Reynolds numbers," *Phys. Fluids* **31**, 057101 (2019).